Multi-objective Aerodynamic Assessment and Optimisation of Winglets for the Flying-V Aircraft Configuration

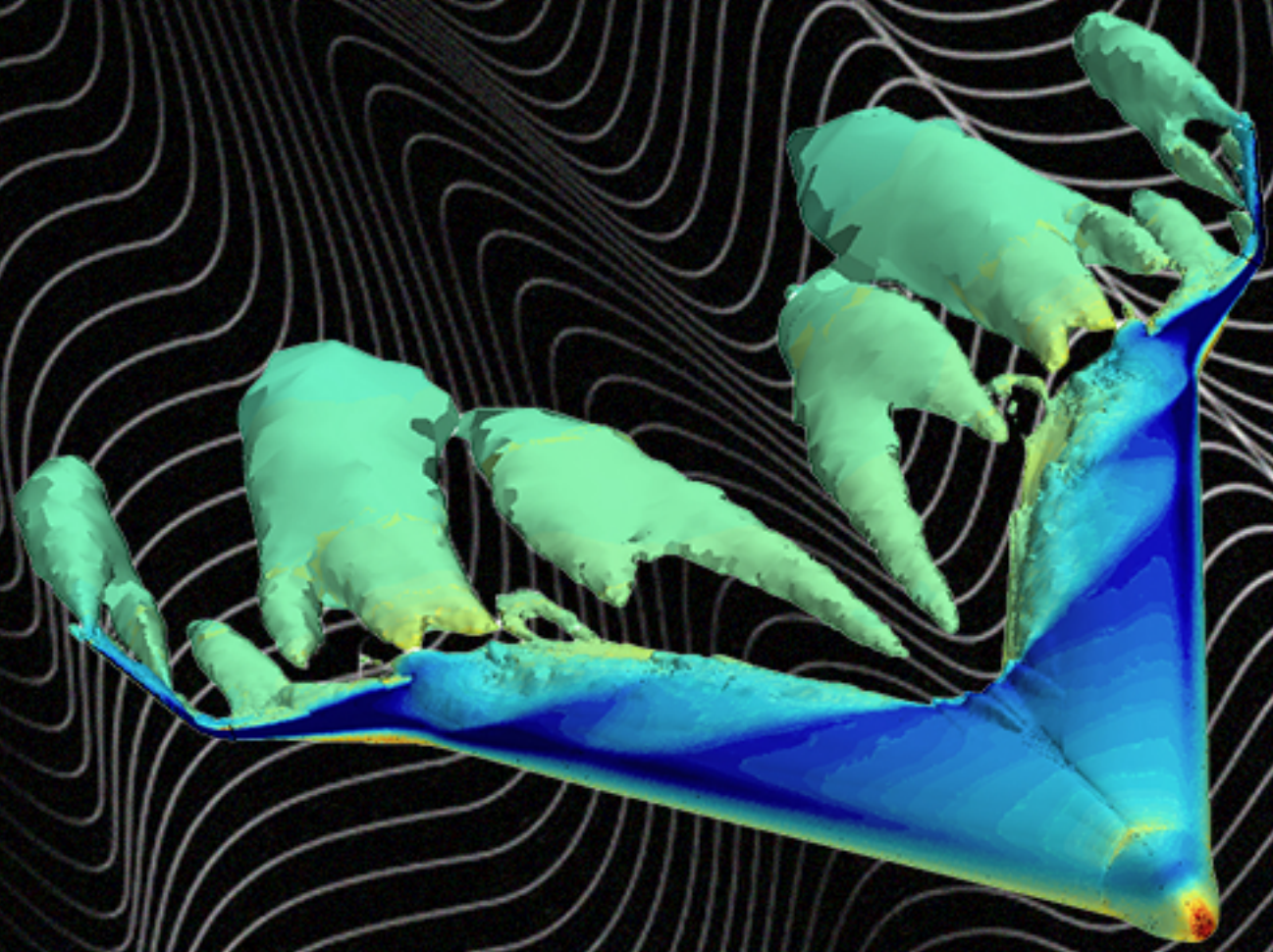

Delft University of Technology

TU Delft

Arjav Anand Amur

Multi-objective Aerodynamic Assessment and Optimization of Winglets for the Flying-V Aircraft Configuration

by

Arjav Anand Amur

to obtain the degree of Master of Science
at the Delft University of Technology
to be defended publicly on May 24, 2023 at 13:00

Student number:	4890760
Project Duration:	September 2021 - May 2023
Place:	Faculty of Aerospace Engineering, TU Delft
Supervisor:	Dr. ir. R. Vos
Thesis committee:	

Dr. ir. R. Vos	TU Delft, Chair
Dr. ir. T. Sinnige	TU Delft, Examiner
Dr. ir. M. I. Gerritsma	TU Delft, External Examiner

An electronic version of this thesis is available at http://repository.tudelft.nl/.

TU Delft

In the loving memory of Ajja

"It is a little wing. That's why I called them winglets. It's designed with all the care that a wing was designed."

— Richard Travis Whitcomb
NASA Langley Research Center,
1976

Abstract

The Flying-V is a disruptive flying wing aircraft configuration that was realized at the Airbus Future Projects Office (FPO), with research and development continuing at TU Delft. Preliminary findings have indicated that the Flying-V is 25% more aerodynamically efficient than the state-of-the-art Airbus A350. To further reap the benefits of this configuration, the aerodynamic design of every element of the Outer Mould Line (OML) must be refined to maximize performance during cruise flight. One such element is the wingtip device, specifically the winglet, which are non-planar wings that can significantly reduce the lift-induced drag of an aircraft. For the Flying-V, the winglets also double as vertical stabilizers. A numerical experiment was conducted to evaluate and augment the lateral-directional stability and aerodynamic performance of the Flying-V, incorporating a contemporary winglet design. To enable the winglet's equally weighted multi-objective optimization, a dedicated module was developed for the existing Flying-V design framework. This module comprises an automated geometry generator, spatial discretizer, flow solver and a differential evolution-based optimizer. For all purposes, the turbulent flow field around the aircraft was resolved using the Reynolds-averaged Navier-Stokes (RANS) model. The Morris method was employed to analyse the sensitivities of the cost functions to the design parameters, yielding an improved baseline design from the ensuing sampling study. The optimization was performed sequentially with complementary planform and airfoil optimization steps. The cruise efficiency of the Flying-V with the initial winglet is found to be lower than the winglet-off case despite portraying strong stability characteristics during approach conditions. While the baseline design's efficiency is enhanced relative to the winglet-off scenario, the stability performance drops from the initial design. A considerable improvement is obtained in both objectives from the planform optimization process, with the optimizer favouring stability slightly more than efficiency. The airfoil optimization results in a design that is not significantly better than the planform-optimized design in stability and aerodynamic objectives.

Preface

The work that follows would not be possible without the support and love of all the wonderful people involved. I am grateful to Professor Roelof Vos for giving me the opportunity to work on the Flying-V and taking the time to define a project that suited my interests. His ideas and feedback really opened up the directions I could take with my thesis and helped me shape this research into its current state. You have always delivered on resources and assistance I have requested as quickly as you could, which is more than what any student could ever ask for. I hope I have not been too much of a menace in your academic life in these past years.

I would like to extend my gratitude to Dr Justus Benad for guiding me through the project when I could not reach Professor Roelof. Although our meetings were brief, your ideas and recommendations really contributed to a fundamental part of my thesis. I thank Professor Marc Gerritsma and Professor Tomas Sinnige for agreeing to be on my committee, and Professor Tomas for also letting me use the computer in his office for my optimization runs. On the same note, I show my appreciation to Professor Alexander van Zuijlen for providing me with access to the high-performance computing facilities at the aerospace faculty and showing me the ropes. I am thankful to Max Baan from ParaPy for helping me with questions regarding ParaPy and the timely renewal of my (many) licenses; And my fellow student Julien Okinine for giving me a crash course on ParaPy's web-based functionalities and parallel processing methods, and taking the time to brainstorm with me on the different ways I could structure my optimization framework. I thank Pieter-Jan Proesmans for helping me get set up with the Flying-V repository and for going out of his way to help me fix issues I was facing with meshing and SU2. I express my deepest gratitude to Susan de Rouw for helping me with problems I was facing as a student and for checking up on me and my mental state of health every now and then. It was always uplifting to have a listening ear to vent my frustrations.

A big chunk of my time as a thesis student was spent working at Maeve (or Venturi as we started off as). My weekly days at Maeve were a stimulating and intellectual distraction from thesis work. I like to think that my work there and my thesis were complementary to each other. They only made me a better engineer and either project more appreciable. I am genuinely grateful to all my colleagues, past and present, for the time spent together and the lessons learnt. I cannot forget to thank all my homies and housemates across Delft for the roasts, the toasts, the ridiculously amusing times, and for always being there for each other.

Last but certainly not least, words cannot express my gratitude to my family for their unconditional love and support. Amma and Appa, none of this would be possible without you, I would not be possible without you. The biggest shout out to my little sister for the coolest cover pages on the block for all my reports as a research student. Seeing your work only inspired me to be better at mine.

— Arjav Amur
Delft, The Netherlands,
2023

Contents

Nomenclature

Acronyms

ACARE	Advisory Council for Aeronautics Research in Europe
API	Application Programming Interface
CG	Centre of Gravity
CST	Class-shape Transformation
DE	Differential Evolution
EASA	European Union Aviation Safety Agency
EE	Elementary Effects
FPO	Future Projects Office
FV-1000	Flying-V 1000 Variant
HLP	High Level Primitives
HPC	High-performance Computing
JST	Jameson-Schmidt-Turkel
KBE	Knowledge Based Engineering
LHS	Latin Hypercube Sampling
MDD	Design Dive Mach Number
MLW	Maximum Landing Weight
MMG	Multi-model Generator
NASA	National Aeronautics and Space Administration
OAT	One-at-a-time
OEI	One Engine Inoperative
OML	Outer Mould Line
OOP	Object-oriented Programming
RANS	Reynolds Averaged Navier-Stokes Equations
SA	Spalart-Allmaras
SU2	Stanford University Unstructured

Greek Symbols

α	Angle of Attack	[°]
β	Sideslip Angle	[°]
$\mathbf{\Pi}$	Matrix of Design Variable Trajectories	[-]
$\Delta\eta$	Fraction of Winglet Span	[-]
δ	Control Surface Deflection or Thickness	[° or m]
ϵ	Twist Angle or Error	[° or %]
η	Spanwise Location as a Fraction of Wing or Winglet Span	[-]
Λ	Leading Edge Sweep Angle	[°]
λ	Taper Ratio	[-]
μ	Mean	[-]
ϕ	Cant Angle	[°]
σ	Standard Deviation	[-]
$\vec{\tau}$	Tangent Vector	[-]
$\vec{\zeta}$	Direction Vector	[-]

Latin Symbols

(t/c)	Thickness to Chord Ratio	[-]
(x/c)	Winglet or Wing Chord Fraction	[-]
$\boldsymbol{A}$	Matrix of CST Coefficients	[-]
$\boldsymbol{X}$	Matrix of Design Variables	[-]
$\overline{c}$	Mean Chord	[m]
$\vec{d}$	Semi-elliptic Curve Conjugate Diameter	[m]
$\vec{x}$	Coordinate Vector	[-]
a	Kuchemann Tip Curvature Factor	[-]
b	Winglet or Wing Span	[m]
C	Coefficient	[-]
D	Drag	[N]
E	Elementary Effect	[-]
e	Exponential Constant	[-]
f	Objective or Cost Function	[-]
g	Penalty Function	[-]
H	Altitude	[m]
I	Moment of Inertia	$[\mathrm{kg} \cdot \mathrm{m}^2]$
i	Index	[-]
j	Component of Objective Function or Index	[-]
L	Lift	[N]
M	Mach Number	[-]
n	Spanwise Kuchemann Tip Sections or Number of Mesh Elements	[-]
o	Order of Kuchemann Tip Parabolic Curve	[-]
p	Penalty Factor	[-]
r	Shape Parameter for Rounded Wing Tip or Radius	[- or m]
Re	Reynolds Number	[-]
S	Surface Area	$[\mathrm{m}^2]$
t	Normalized Chordwise Location for Rounded Wing Tip	[-]
V	Airspeed	$[\mathrm{m} \cdot \mathrm{s}^{-1}]$
w	Weighting Factor	[-]
x	Position along the X - Axis	[m]
y	Position along the Y - Axis	[m]
$Y+$	Normalized Wall Distance	[-]
z	Position along the Z - Axis	[m]

Subscripts or Superscripts

$*$	Absolute	[-]
0	Centroid	[-]
1	Minor Diameter or Index	[m]
2	Major Diameter or Index	[m]
3	Index	[-]
a	Aerodynamic	[-]
b	Blend Section	[-]
D	Drag	[N]
des	Design	[-]
dyn	Dynamic	[-]
f	Friction	[-]
fin	Vertical Tail or Winglet	[-]
L	Lower or Lift	[- or N]
l	Rolling Moment or lower	[N · m or -]
LE	Leading Edge	[-]
n	Yawing Moment	[N · m]
p	Pressure	[-]
r	Root or rudder	[-]
ref	Reference	[-]
t	Tip	[-]
TE	Trailing Edge	[-]
U	Upper	[-]
u	Upper	[-]
w	Wetted	[-]
wt	Winglet	[-]
x	Function of Position along the X - Axis	[m]
y	Side Force	[N]

List of Tables

List of Figures

Chapter 1

Introduction

With the advent of air transportation, a new source of emissions was introduced to the already significant contributions to anthropogenic climate forcing by the industrial revolution. Since its initiation in the 1920s [1], the commercial aviation industry has grown by over 1400 % [1] and is projected to rise even further. Efforts to diminish the impact of aviation on climate change necessitate a rapid escalation in the fuel efficiency of aircraft and their systems. Historical trends to achieve such growth have been targeted towards the three pillars of airplane design—aerodynamics, propulsion and structures [2]. Aerodynamic efficiencies have increased by 15 %, averaging 0.4 % per year, but are beginning to stagnate [2]. The focus on gaining increments in the aerodynamic performance of aircraft has mainly been oriented towards cleaner wing designs with improved engine installation [2]. However, to reach the necessary aerodynamic efficiencies, a radical change in the configuration of aircraft is vital. Integrated wing-body designs like the blended wing-body and flying wing concepts have proven capacity to satisfy these requirements in the past. Liebeck [3], Smith [4], and Bolsunovsky et al. [5], to name a few, demonstrated lower fuel burn per seat kilometre, reductions in take-off weight and adaptability to higher cruise Mach numbers resulting from these aerodynamically superior design configurations compared to classical tube and wing setups.

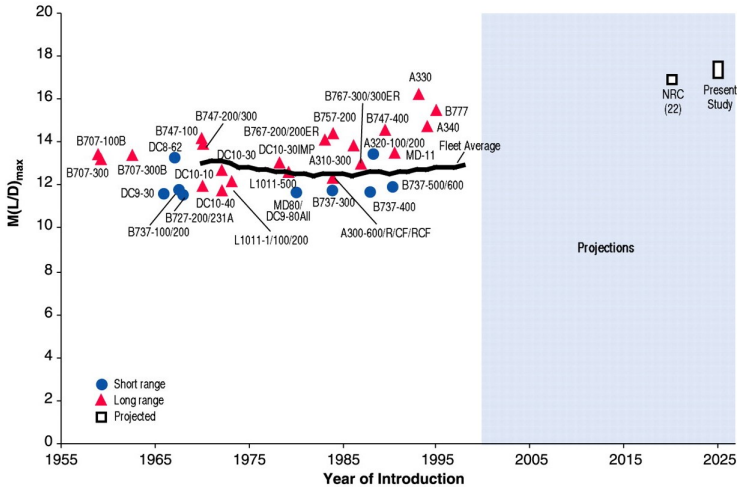

Figure 1.1: Historical and Projected Trends in Aerodynamic Efficiency of Commercial Aircraft [2]

A novel idea within the realm of flying wings took shape at the Airbus Future Projects Office (FPO) in 2015. Benad [6] established a configuration concept that could efficiently allocate volume inside a flying wing for commercial aviation operations. He proposed obliquely combining two structurally efficient cylindrical

[1] The World Bank. *Air transport, passengers carried* Retrieved 5 May, 2023 from `https://data.worldbank.org/indicator/IS.AIR.PSGR?end=2020&start=1970&view=chart`

pressure vessels at the nose along the longitudinal axis of an aircraft to form an inverted 'V' shape. Due to this, the configuration was designated the Flying-V. The angle between the two modified cylinders can be adjusted to conform to a wing leading edge sweep angle, such that a wing could then be wrapped around it. A streamwise cross-section of this arrangement leads to a typical airfoil shape, providing the same design flexibility as a typical wing. The wing planform is characteristic of a cranked-arrow wing, with a highly swept inboard wing and an outboard wing with a lower sweep as seen in Figure 1.2b. The outboard wings extend vertically to form winglets that also function as the vertical stabilizer. Directional control is provided by rudders placed on the winglets, and elevons placed on the outboard wing control lateral and longitudinal manoeuvrability. It was hypothesized that placing the two turbofan engines on the suction side of the wings as shown in Figure 1.2b could lead to a lower nose profile due to a shielding effect. For similar cruise conditions and payload capacity as the state-of-the-art tube and wing aircraft Airbus A350-900 [2], the conceptual study showed that this Flying-V configuration exceeded the aerodynamic performance by 10% and has the potential to meet the short term goals set forth by the Advisory Council for Aeronautics Research in Europe (ACARE). [3], and could possibly represent an inflection point in the design trend of commercially viable aircraft since the 1950s. The preliminary design of the Flying-V is currently underway at the Delft University of Technology. The following section provides a brief introduction to the design work that has followed at TU Delft in the context of this research.

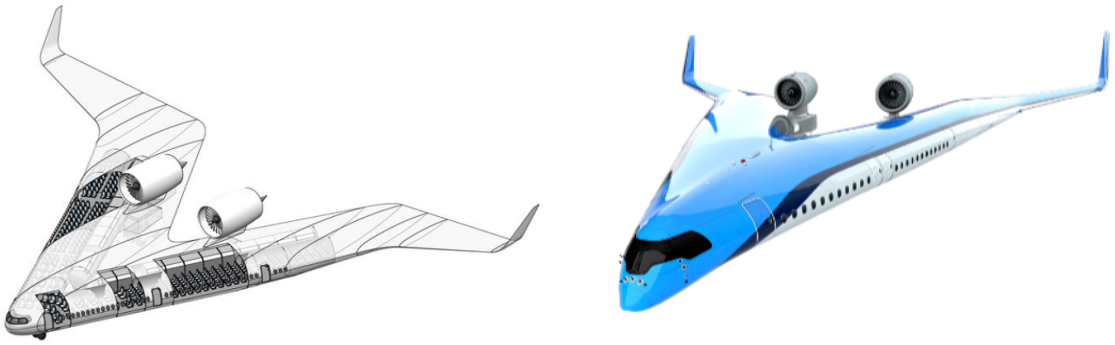

(a) (b)

Figure 1.2: Flying-V Concept (left) by Benad [6], and (right) the Flying-V Render at the TU Delft [4]

1.1 The Flying at TU Delft

The geometry of the Flying-V aircraft has undergone a number of changes since Benad's [6] initial proposal, most significantly oriented towards the wing and fuselage. In order to estimate the aerodynamic performance potential of Benad's [6] Flying-V, Faggiano [7] set out to find an optimum for this configuration through a variable fidelity design space search. The result of this study was a re-defined outer mould line (OML) and cabin configuration. The work of Faggiano [7] also resulted in a Flying-V OML with a maximum aerodynamic efficiency of 23.7 in cruise, exceeding the performance of a state-of-the-art A350-900 reference aircraft by 25%. Compared to Benad's [6] design, the new OML exhibited lower wave and vortex drag components and the pitching moment was constrained. The lift distribution obtained was almost elliptic by aligning the isobar close to the root and reducing supersonic flow regions on the outboard wing [7]. Subsequent studies performed using this newly optimized OML led to the re-parameterization of the Flying-V configuration; First, as a result

[2] Airbus Aircraft. *A350-900 - Shaping the future of air travel* Retrieved 5 May 2023 from `https://aircraft.airbus.com/en/aircraft/a350-clean-sheet-clean-start/a350-900`

[3] Advisory Council for Aviation Research and Innovation in Europe *Achieving climate neutral air mobility* Retrieved 5 May 2023 from `https://www.acare4europe.org/acare-goals/`

[4] Flying-V. *Energy-efficient flying over long distances* Retrieved 12 May, 2023 from `https://www.tudelft.nl/lr/flying-v`

of a study by Hillen [8] to include cabin design flexibility and manufacturability, at the same time being able to be used in an aerodynamic optimization routine. And second, while in the due process of assessing the capability of the Flying-V design to be scaled into a family of aircraft, as researched by Oosterom [9]. Post the re-parameterization of the OML, Hillen [8] also re-analysed the OML with planform and airfoil shapes that closely resembled that of Faggiano's [7]. The resulting pressure contours on the new parameterization are shown in Figure 1.3b. A drop of 15% was noticed in cruise flight aerodynamic efficiency with the new structurally attractive parameterization. The optimized design by Faggiano did not feature a cockpit or centre fairing design but rather a port wing and its mirrored component meeting at the longitudinal symmetry plane. In addition, the design was prone to a strong root effect owing to the highly swept inboard wing, where the isobars were twisted towards the trailing edge causing strong shock-induced separation and a drop in the lift at this section. Pluijm [10] was able to crystallize a parameterization while satisfying constraints set by pilot anthropometry and visibility, positioning of the nose landing gear and weather radar, with satisfactory aerodynamic performance.

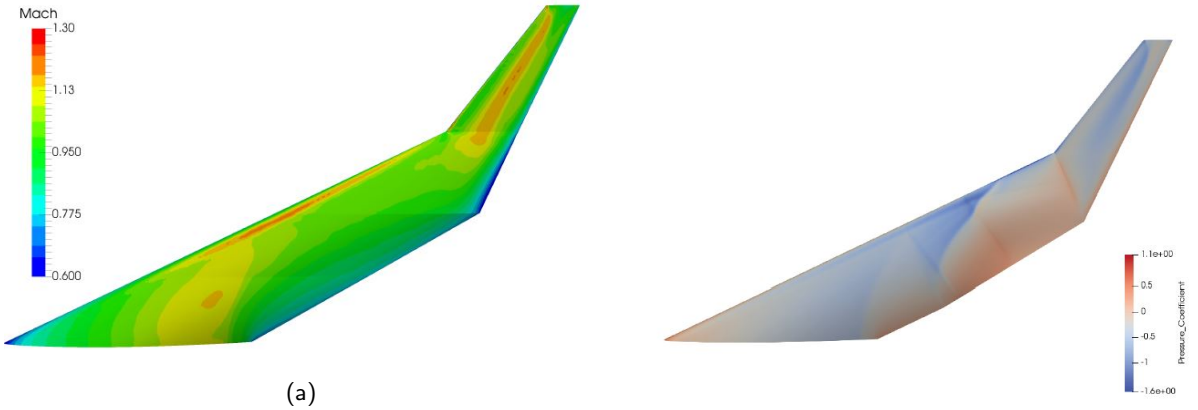

(a) (b)

Figure 1.3: Comparison of Aerodynamic Results at Cruise Resulting from the Parameterizations of Faggiano [7] (left) and Hillen [8] (right)

The initial design by Benad [6] featured winglets for the primary purpose of directional stability and control. The winglets were sized to meet minimum requirements of directional stability, leading to winglets with a total projected area S_{fin} of 16 $[\text{m}^2]$. Faggiano [7] crudely parameterized the winglets considering more specific driving requirements such as the static directional stability, one engine inoperative condition (OEI) at take-off, and landing in maximum cross-wind condition. A further parameterization of the winglets was made in the due course of building the wind tunnel model of the Flying-V by Johnson [11]. He found that integrating the winglets improved and decreased the aerodynamic efficiency in different scenarios but almost always reduced it when the rudder was deflected. During a handling qualities assessment of the preliminary Flying-V design, it was found that the Flying-V displayed unsatisfactory lateral-directional stability though the yawing moment coefficient due to sideslip C_{n_β} and rolling moment coefficient due to sideslip C_{l_β} were positive and negative respectively for all configurations [12]. It was also found that except for one condition, the Flying-V poses strong Dutch roll tendencies, requiring the use of a yaw damper. The Flying-V's rudder control power was lacking during a coordinated turn in OEI conditions with the forward centre of gravity (CG) limit at maximum landing weight (MLW) close to approach speeds [12]. A simulation of the bank-to-bank manoeuvre [13] at approach speeds required excessive rudder deflections [12]. Finally, a steady heading sideslip, in particular, an OEI climb requirement [13] manoeuvre simulation of the Flying-V, uncovered requirements in rudder deflections beyond the design limit, further showing the limited lateral-directional control power of the Flying-V. To resolve

these issues a detailed definition of winglets was established by Horwitz [14]. This parameterization includes only winglet planform variables. The blend radius r_b, the winglet twist angle and the sectional profiles were not considered in this study as they did not pose significant sensitivity towards stability and control characteristics. The winglets' section profiles used by all researchers were the airfoil section used for the wing tip. A more refined design for the winglets was also found by creating a surrogate aerodynamic model using the kriging approach for feasible winglet designs in approach conditions. A winglet design was recommended from the 50 variants tested, that meets the target values for lateral-directional stability, exhibits no roll reversal, and increases aerodynamic efficiency by 13.4% but fails to meet the target yawing moment due to rudder deflection requirements.

1.2 Problem Statement

Considering the multiple reports of a lack of performance in both the cruise aerodynamic efficiency and lateral-directional stability of the Flying-V configuration, the potential to investigate the source of the bad performance and to improve upon it exists. Additionally, the validity of the previous findings on the lateral-directional stability and control in approach conditions and the aerodynamic efficiency in cruise must be supplemented with higher fidelity information. This also requires adding more detail to the geometric parameterization of the Flying-V, for instance, the control surfaces. The purview of the present work will be limited to the winglets and the rudder. The main objective of the current research is:

To reconfigure the winglet geometry of the Flying-V simultaneously for enhanced aerodynamic and lateral-directional stability performance, using RANS-based aerodynamic analysis and shape optimization methodologies.

The following research questions are identified to guide the research to meet the objective.

1. What design for the multi-functional winglets of the Flying-V maximizes aerodynamic performance and stability requirements?
    (a) What is the maximum cruise flight aerodynamic efficiency increase that can be obtained with the optimal winglets compared to the baseline winglet-off Flying-V?
    (b) What is the maximum lateral-directional stability increase that can be obtained in approach conditions with the optimal winglets compared to the Flying-V with the initial winglet design?
    (c) Which performance parameter uniquely captures the coupled effect of lateral-directional characteristics of an aircraft?
    (d) How does a minimum thickness structural constraint influence the optimal geometry?
2. What is the performance of the Flying-V's rudder in varying steady heading sideslip conditions?
    (a) How must the rudder be parameterized for the unconventional vertical tails?
    (b) How does the rudder perform at a defined maximum rudder deflection?

1.3 Outline of the Thesis

The following research is structured as follows: chapter 2 provides the reader with a literature overview on the topic of this research; chapter 3 describes the setup and the steps taken for the numerical experiment while chapter 4 explains the verification and validation process undertaken. Finally, chapter 5, chapter 6, and chapter 7 provide an extensive breakdown of the outcomes of this research and recommend research possibilities for the future.

Chapter 2

Background

The following chapter briefly introduces the flow phenomenon over and behind a wing that introduces a source of loss to its aerodynamic efficiency and a solution used to mitigate this. The evolution, pros, and cons of this solution and the best design practices collected from impactful research in the past are also provided in the setting of the Flying-V aircraft.

2.1 Induced Drag and the Need for Wing Tip Devices

By virtue of the pressure gradient between the suction and the pressure side, the basis for the generation of lift, a discontinuity in the pressure balance exists as one moves from the wing root towards the tip [15]. This discontinuity induces a flow around the tip of the wing from the lower side to the upper side of the wing surface and in conjunction with the freestream velocity a swirl component is generated, resulting in continuous wing tip vortices being shed from the tip of the wing [15]. A consequence of this is a cross-flow component in the spanwise direction, induced along the top and bottom surfaces of the wing [15]. On the suction side, this cross-flow component is in the direction of the root of the wing, which leads to the streamlines bending towards the inboard section [15]. On the pressure side, the cross-flow component directed towards the wing tip leads to the streamlines bending in the outboard direction [15].

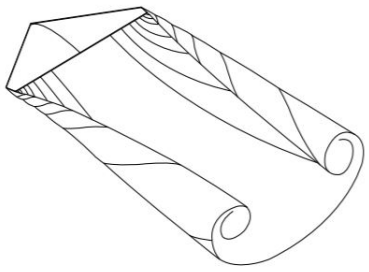

Figure 2.1: The Resulting Wake Behind a Lifting Wing [17]

These shed vortices in conjunction with the wake from the trailing edge of the wing results in a vortex sheet that rolls up towards the wing root, with two distinct vortex cores as shown in Figure 2.1. Mclean [17] explains that a common misunderstanding of this flow is that these vortex sheets are a result of the global flow pattern, but are rather just a manifestation. The vorticity that is fed into these vortex cores is contributed by the entire wing span and not just the wing tips [17]. Consequently, this global flow pattern downstream of the wing induces a downdraft or a downwash that results in a downward velocity component, which reduces the angle of attack seen by the wing sections by a certain magnitude [15]. The angle by which the effective angle

of attack is reduced is called the induced angle of attack and causes a component of the lift force to act in the freestream direction, i.e., a drag force. This drag force is called the induced drag [15]. The existence of this drag force can also be thought of as a consequence of a pressure imbalance in the freestream direction [15], with reduced pressure downstream of the wing [17]. To prevent unfeasible wing structural requirements and to satisfy operational constraints, arising from the need for long slender wings as a solution for induced drag reductions, wing-tip devices such as rounded tips, raked tips, Hoerner tips and non-planar wing tips are often used. Non-planar wing tips like winglets provide greater improvements in induced efficiency compared to planar tip extensions like the Hoerner and raked tips [17].

2.2 Design of Winglets

The earliest accounts of aerodynamic benefits of non-planar wing tips like end-plates come from Frederick W. Lanchester [23] who published a qualitative analysis of the 3D flow around the wing including the effects of the vortex wake behind the wing. Patents for such vertical wing tip devices were obtained much earlier in 1897 by Lanchester himself even before the first controlled flight [18]. These analyses and benefits were further substantiated when Ludwig Prandtl developed his lifting-line theory [24] in 1918 which provided a deeper understanding of induced drag. Since then many theoretical studies, most notably by Nagel [26] in 1924, Mangler [27] in 1938, and Weber [28] in 1954 independently studied the effects of end plates and vertical plates on the span load distribution and induced drag. Although many experimental campaigns that ensued from these findings showed aerodynamic benefits at high-lift conditions, the practicality of non-planar surfaces was deemed inconsequential due to the offsetting penalties in profile drag at high subsonic speeds [29]. With the growing need for improvements in fuel efficiency during the oil crisis in the 1970s [16], a series of exploratory studies on non-planar wingtips was initiated by a team of researchers led by Richard T. Whitcomb at the National Aeronautics and Space Administration (NASA). The program included theoretical and experimental studies at the eight-foot transonic pressure wind tunnel at Langley Research Center at NASA [29]. Whitcomb and his team formalized a fundamental knowledge base and design approaches for what they termed winglets, due to the attractive benefits they provided to improve the aerodynamic efficiency at the design point of civil and military aircraft. What was different from earlier findings that led to these conclusions was that Whitcomb considered the design of these wing tips as though they were wings [29]. In-flight evaluations were first conducted on the KC-135 by NASA and the US Air Force to test this new concept, due to the higher loading on its wing tips. This was followed by flight tests on the DC-10 by Mcdonnell Douglas with and without winglets. Both programs yielded the same results as was ascertained by previous wind tunnel tests, but were not applied to operational fleets due to higher recertification costs estimated by Douglas and the Air Force prioritizing newer, more efficient engines over the winglets.

2.2.1 Design for Vortex Drag Reduction

A central factor that has been underlined by many impactful studies [16], [17], [18], [19], [20], [22] in the design of winglets is that the offsetting penalties (as identified in the previous section) must be constrained as much as possible to obtain a positive net aerodynamic performance improvement. For example, on more practical designs, the span load is distributed such that more load is applied on the inboard wing than the outboard wing, to restrain a large increase in bending loads even though an ideal span loading for reduced induced drag warrants an even distribution [17]. The complexity of the flow field behind the winglet for a given wing design often makes a generic design recommendation for winglets impossible. Most design studies aim to reduce the strength or relocate the tip vortices to allow a favourable flow on the wing and other components, and attempt to produce a strong forward component of the flow, a thrust force [19], [18], [17]. Still, some fundamental theories of lift based on on first principles often provide insight into the optimal design of winglets.

Munk [25] in 1923, laid down the theory for minimum induced drag based on Prandtl's lifting line theory. He found that by limiting the roll-up of the vortices along the wing, the amount of induced drag produced could be minimized. He mathematically proved for both planar and non-planar wings that the downwash profile on the wing was a function of the dihedral angle of the wing [25]. This led to the later validated design principle that the variation of the cant angle can produce significant induced drag reductions [18], [20].

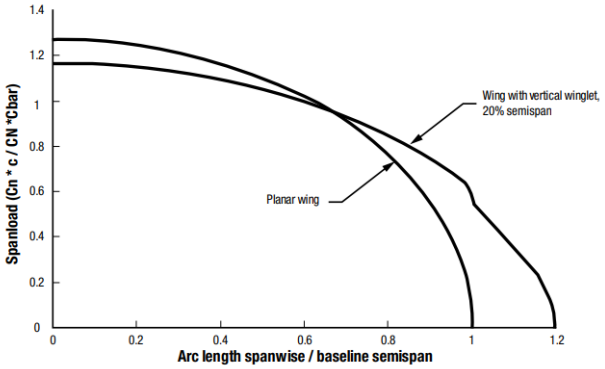

Figure 2.2: Example of an Ideal Lift Distribution for a Wing with a Winglet [17]

Most early winglet designs incorporated a simple canted non-planar wing as a winglet in order to reduce the complexity of the design at the wing tip and reduce the wingtip loading to prevent the corresponding structural weight increase [18]. To add to this was the fact that most winglets were retrofitted at the time [17]. The chord distribution between the wing and the winglet, although did not feature a smooth distribution (blending), often was discontinuous, but did not change abruptly, as this was found to induce separation at the junction of the wing-winglet, leading to an early vortex formation, more inboard of the wing [31], [18], [36]. On more modern designs, the concept of blending was introduced, to ensure a geometrically continuous surface between the wing and the winglet. The wing tip chord is often set equal to the wing root chord, with a certain conic-section distribution given to the blended surface [31], [22]. This reduces the possibility of super velocities being formed at the blended junction and gives more freedom to align the isobar pattern between the wing and the winglet. In other words, the generation of shocks and the prevention of shock-induced separation is often the focus for this part of the winglet design [22], [31].

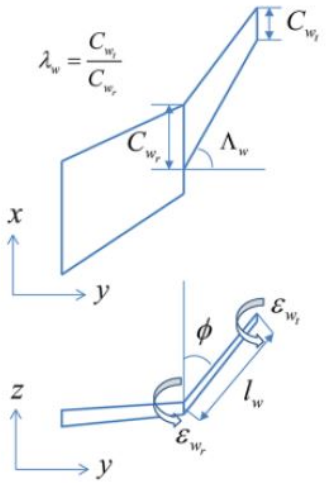

Parameter	Description	Unit
b_{wt}	Winglet Span	[m]
c_{wt_r}	Winglet Root Chord	[m]
λ_{wt}	Winglet Taper Ratio	[m]
Λ_{wt}	Winglet Leading Edge Sweep Angle	[°]
ϵ_{wt_r}	Winglet Toe Angle	[°]
ϵ_{wt_t}	Winglet Tip Twist Angle	[°]
ϕ_{wt}	Cant Angle	[°]

Figure 2.3: Geometry (left) and Commonly Used Winglet Design Parameters (right) [32]

The geometry of winglets is often parameterized on a case-specific basis according to the needs of the wing design. But a generic design parameterization for a single fin blended winglet can be identified from literature [18], [20]. This generic parameterization (Figure 2.3) often prioritizes a smooth transition from the wing to the winglet, to ensure that the leading and trailing edges produce a C1 or higher curve continuity [20]. Many winglet parameterization and optimization studies avoid the use of airfoil shapes in their work and often resort to using the airfoil shape from the wing or the design conceptualized by Whitcomb [18]. This helps reduce the dimensionality of the optimization problem and makes the design less complex when considering the surface continuity, especially at high winglet cant angles. If the airfoil shapes are to be included in the shape definition a low-order parameterization such as the class-shape transformation [41] or the PARSEC method [21] is often used [20]. Although the winglet root and tip twist angles provide the ability to tweak the spanwise lift distribution, the effect on the overall performance of the winglet is often marginal [30].

2.2.2 Design for Lateral-Directional Stability and Control

Since winglets are generally sized and designed to provide aerodynamic benefits on an aircraft, the number of dedicated work to also include directional and/or lateral objectives is limited. Although the coupled nature seems unconventional, systems have been designed in the past to meet the disparate objectives individually for conventional aircraft. The effects of different non-planar shapes have been studied for aerodynamic benefits, and non-planar non-lifting surfaces that provide directional-lateral stability, called vertical stabilizers are a critical stability and control system on conventional aircraft. The driving requirements for lateral-directional stability imposed on conventional vertical tails can also be used to impose design constraints on the stability requirements of the Flying-V's winglets. This was also the approach that was taken by previous researchers [7], [12], [14] for the flying-V. According to Obert [16] the primary function of a vertical stabilizer is to provide large contributions to static and dynamic lateral-directional control and stability. This capability must be possible even at limiting cases such as those encountered during high angles of attack and angles of sideslip, possibly due to an OEI scenario or large crosswinds. The control capability the system provides must be possible with acceptable stick forces, such that the pilot must be able to balance the aircraft in extremely destabilizing conditions.

In the context of unconventional aircraft configurations, blended wing bodies and flying wings are known to have pronounced issues in lateral-directionally stability [5]. The highly integrated designs of these aircraft lead to relatively lower moment arms and lower control volume available to build an inherently stable aircraft[5]. Yaw-control integrated winglets are often an attractive design choice since they allow the possibility for sufficient lateral-directional control without sacrificing the trailing edge span required for longitudinal control [36]. Coupling the two functionalities also provides the added benefit of a lack of drag penalty associated with the addition of a vertical tail [36]. Hageman [36] devised a yaw-integrated winglet design routine for a blended wing body design to investigate the effect of the dual functions on its design. Similar to the results of the study by Cappuyns [12] he found the winglets to provide a statically stable aircraft in some lateral-directionally perturbed conditions but found that none of the 400 designs tested could suppress the Dutch roll mode. Bourdin et al. [37] investigated a novel control technique on a flying wing where each winglet could attain varying cant angles at different flight conditions. Using panel methods and wind tunnel tests, they found that the relative deflection required to attain the same level of stabilizing moments compared to a symmetric flight control model was significantly lower. Although, due to the segregated control allocation, they anticipated that the design of such a control system could be highly complicated due to the multi-axis coupled moments that were encountered in such scenarios.

A number of studies found the positive contribution of winglets to lateral-directional stability and handling

qualities. Wind tunnel tests were conducted to investigate the use of winglets as a directional control device for aircraft by Jordan et al. [33]. The tests were performed on a generic transport model with and without winglets, and the results showed that the winglets improved directional stability and control. The authors suggest that the effectiveness of the winglets for directional control is due to the fact that they increase the effective span of the aircraft, thereby increasing its directional stability. The paper concludes that winglets can be a viable option for improving directional control in aircraft, especially for applications where other control surfaces may not be feasible due to space or weight limitations. Sohovic [34] performed flight tests to evaluate the effect of winglets on the handling qualities of an aircraft. A modified Learjet 25D was used with and without winglets, and the results showed that the winglets improved the aircraft's directional stability and control, particularly at high speeds and high altitudes. They concluded that winglets can be a valuable addition to aircraft for improving handling qualities, especially in high-performance applications. Holmes et al. [35] also conducted flight evaluations on a single-engine general aviation aircraft with winglets to test their effects on the flight performance and handling qualities as compared to a winglet-off aircraft in cruise and approach conditions. They found that the roll rate was increased for a given rudder input and that the lateral control using only rudders was vastly improved. They also noticed a 50 % improvement in the side force due to sideslip of the aircraft and found no non-linearities in the range of operational sideslip angles during steady heading sideslip conditions. It was easier for the aircraft with winglets to get out of an adverse yaw condition than the aircraft without winglets. The winglet-configured aircraft did not noticeably improve the spiral or dutch-roll modes but also mention that they found winglets on non-swept wings to have insignificant effects on the yawing moment due to sideslip C_{n_β}. Finally, during a stall, they noticed the winglet-off configured aircraft had a tendency to drop a wing or roll-off, which was greatly reduced on the aircraft with winglets.

2.3 Benefits and Costs of Winglets

Mclean [17] identifies a number of positive elements that come with the inclusion of winglets in an aircraft's design. In addition to the reduction of induced drag in cruise and/or take-off, a decrease in wave drag can sometimes be expected due to the change in the lift distribution of the wing. From an operational viewpoint, aside from the obvious facts that fuel burn is reduced and the design range can be extended, a shortening of the take-off field length can be produced if the winglets are designed to operate optimally in the second climb segment [17], [22]. Additionally, aeroelastic tailoring of the wing with the winglet can stretch the buffet margin providing scope for a higher cruise altitude, and cruise speed due to an increase in the design dive Mach number (MDD). From a regulatory aspect, airport gate clearances can be met with minimal restrictions on performance, when compared with wing tip extensions. To add to this, an advantage not commonly cited is that the separation distances in airports for take-off or landing are shortened as the vortex strength is reduced [17] and deflected at an angle [18] that is less inflicting on the following aircraft. Finally, a design advantage winglets pose is that they can also function as vertical stabilizers on tailless aircraft like the Flying-V, allowing for a cleaner aerodynamic design. On the downside, the integration of winglets can induce many penalties on a number of fronts. Aerodynamically, although induced drag can be reduced, an increase in profile drag is certain due to an increase in wetted area [17]. Moreover, if a winglet is designed as an end plate, without blending it into the wing design, the flow close to the junction can produce punishing interference effects [16] even though the induced drag reduction is more compared to a blended winglet layout [17]. A major con, which is also a decisive factor for the use of winglets by most designers, is the increment in weight: Firstly due to the weight of the winglet itself, secondly due to the weight of the fairing attached for blending the winglet into the wing, and lastly due to the increase in wing structural weight to resist the increasing root bending moment and fulfil flutter requirements [17]. For an aircraft design company, considerations of increased development costs and risks associated with adding a winglet into the existing or new design also play a crucial role in the decision criteria.

Chapter 3

Methodology

The Flying-V design framework called the Flying-V multi-model generator (MMG) is a design environment scripted in the dynamic programming language Python. In particular, the ParaPy library [1] is used to enable requisite functionalities for the design process such as modelling, simulation and documentation. ParaPy is built on the fundamental concept of knowledge based engineering (KBE) and automates repetitive tasks which are typical of engineering design processes in a computationally efficient way. For example, instead of having to manually model the geometry of the Flying-V, ParaPy provides objects that are used as containers for Flying-V design parameters which are generated through code. By simply varying the values of these parameters (design variables), a family of Flying-V geometries can be generated. This concept is analogous to classes and instances in Object-oriented Programming (OOP) and hence justifies the choice of using Python. The high-level primitives (HLP) model in KBE is used in MMGs to parametrically define generic top-level systems like the wing, fuselage, tail and engines, which can be adapted for specific applications and combined together to form the system of interest [38]. The MMG was used and contributed to by previous researchers (see Faggiano [7] to Luijk [40]) and is extended with design features and methodologies generated in this study, particularly a Reynolds averaged Navier-Stokes (RANS) based winglet optimization library. This library was further used for the Flying-V's winglet aerodynamic, stability and control assessment and optimization process. The developed library required multiple consecutive and iterative steps to reach a robust state, both from an engineering and practical perspective. These steps, and the optimization process itself including the various modelling procedures, are elaborated on in detail in the following sections.

3.1 Geometry

The winglet parametric model designed by Horwitz [14] is used for the geometry modelling step in the optimization process. The geometry parameterization for the inboard and the outboard wings remained the same as defined by Hillen [8]. In a parallel study by Luijk [40], the original linear trunk parameterization by Hillen [8] was modified with a new non-linear lofting technique called Gordon surfacing to prevent streamwise discontinuities and sharp leading and trailing edge kinks, leading to a G2 continuous surface. This modification was incorporated into the current study as it was found to make the spatial discretization process more efficient and reliable when taking into account the automation required for the optimization process. It must be noted that the optimization was performed by taking the family-optimized Flying-V 1000 (FV-1000) design by Oosterom [9] as the baseline design for the inboard and outboard wings. Finally, the RANS-optimized nose cone and fairing by Brouwer [39] was also integrated into the geometry used for the analysis, as it was hypothesized that the large side area of the nose cone could lead to strong destabilizing yawing moments which could be

[1] ParaPy. *The ParaPy Platform*. Retrieved 23 March, 2023 from `https://www.parapy.nl/features/`

considered as an implicit stability constraint for the optimization process.

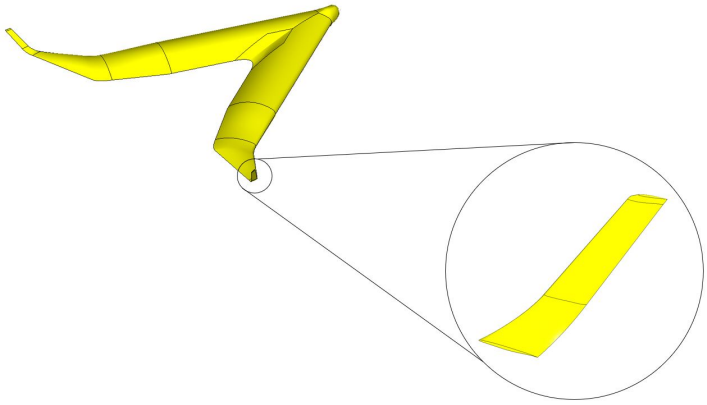

Figure 3.1: Aircraft Geometry used in the Design, Analysis and Optimization of Winglets in this Research

The resulting full aircraft geometry and the focus of attention where changes were made to the geometry are shown in Figure 3.1. The major modifications made include updating the initial design by Horwitz [14] and adding a Kuchemann tip, both oriented towards the RANS analysis and cleaner aerodynamic definition for the winglets. Additionally, rudders were parameterized for the winglets. These modifications and extensions are further elaborated in the following sections.

3.1.1 Winglet Geometry Refinement

A few changes were made to the original parametric geometry model by Horwitz [14]. Firstly, in addition to the design parameters set by Horwitz [14], the winglet root twist (ϵ_t) was added as an additional planform design variable, and instead of using the outer wing tip airfoil as the airfoil for the entire winglet including the blend sections, provisions were made to include a winglet root and tip airfoil, both parameterized through class-shape transformation (CST) parameters [41]. The airfoils on the blend section are therefore now a result of a linear interpolation of the outer wing tip and winglet root airfoils. Secondly, Horwitz [14] used a cylindrical projection of the winglet trunk's leading edge to define the blend trunk's leading edge and trailing edge.

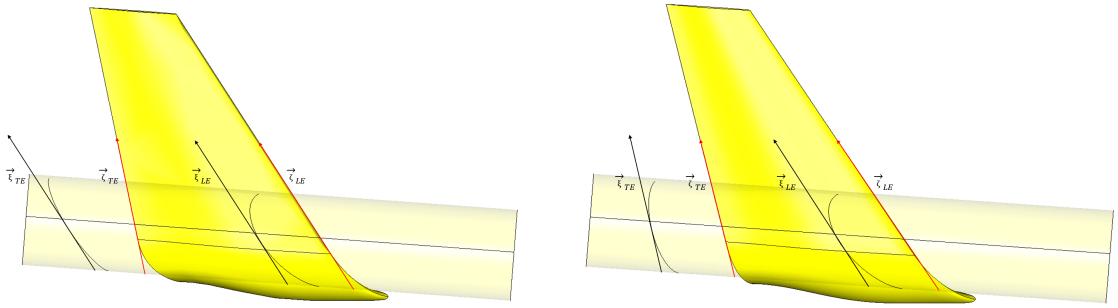

(a) Leading and Trailing Edge Cylindrical Projections by Horwitz [14]

(b) Updated Leading and Trailing Edge Cylindrical Projections

Figure 3.2: Updated Winglet Design

The definition of the trailing and leading edge directions vectors in this case and the resulting cylindrical projections are shown in Figure 3.2a. Where the red lines indicate the direction vectors along the leading and trailing edges and the black lines indicate the direction of the projections. This led to a trailing edge that was C1 continuous as seen in Figure 3.3a, resulting in a highly swept trailing edge definition at the blend section. A change was made to instead take the winglet trunk's trailing edge cylindrical projection to define the blend

trunk's trailing edge. Superimposing this new definition with respect to the direction vectors of the leading and trailing edge onto the cylinder results in projections seen in Figure 3.2b. When the winglet blend section is lofted again, the trailing edge now has a smooth curvature with C2 continuity as shown in Figure 3.3b.

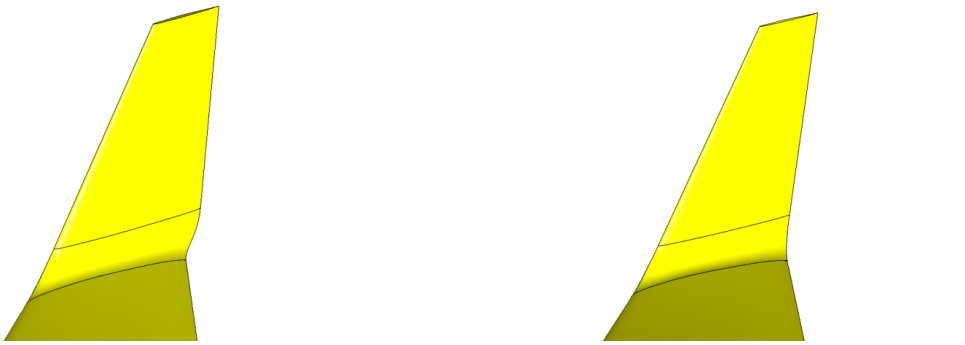

(a) Winglet with C1 Continuous Trailing Edge (b) Winglet with C2 Continuous Trailing Edge

Figure 3.3: Winglet Trailing Edge Continuity Refinement

A consequence on the entire winglet definition now with the updated projections is that the winglet root has lower chord compared to the previous method, and correspondingly the winglet tip as well. This is due to the fact that the projection now sweeps a smaller portion of the cylinder's length as seen when comparing Figure 3.2a and Figure 3.2b. It

3.1.2 Kuchemann Wing Tip Parameterization

The Kuchemann tip is parameterized with a generic class of parabolic curves given by Equation 3.1, which is fit on the leading edge of the winglet. The leading edge points are distributed from the tip of the winglet, along the direction vector $\vec{\zeta_{LE}}$ of the winglet leading edge, resulting in the points being distributed as seen in Figure 3.4a. The planar locations of the leading edge points are ultimately obtained from Equation 3.2. Trailing edge points are also placed along the Kuchemann tip, along the direction vector of the winglet trailing edge $\vec{\zeta_{TE}}$ starting from the winglet tip. The goal was to match the respective vertical locations of the leading and trailing edge as seen in Figure 3.4a. This also ensures C2 continuity between the winglet and the Kuchemann tip. Again, as in the previous section, the red lines indicate the direction vector of the leading and trailing edges. The number of spanwise points n can be defined to allow for as many sections to be placed on the two edges.

$$x = a \cdot y^o \tag{3.1}$$

Where,

$$y = b_{kt} = \Delta\eta_{kt} \cdot b \cdot \vec{\zeta_{LE}} \tag{3.2}$$

The Kuchemann tip span is specified as a fraction of the winglet span $\Delta\eta_{kt}$. A third-order (o) curve is chosen as the baseline for all the winglet cases for the FV-1000, and the curvature factor a is linearly interpolated with respect to the winglet tip chord and the winglet span from various candidate designs generated through a short sampling study. The Kuchemann tip span is confined to 5% of the winglet span as recommended by Kuchemannn [44] as this provides enough room for the tip to bend the isobars towards the tip thereby providing pressure relief behind a shock wave that might exist at the winglet tip. The total span of the winglet is maintained by correcting for the increase in span due to the Kuchemann tip. Curves are fitted to the points that are defined for the leading and trailing edge of the Kuchemann tip- as seen in Figure 3.5a.

These curves are then used as the guiding curves to loft the Kuchemann sections, from the winglet tip airfoil to an airfoil-shaped defined for the Kuchemann tip leading to the Kuchemann tip section seen in Figure 3.4b and Figure 3.5b. The Gordon surfacing technique used by Luijk [40] is also used in lofting the Kuchemann tip.

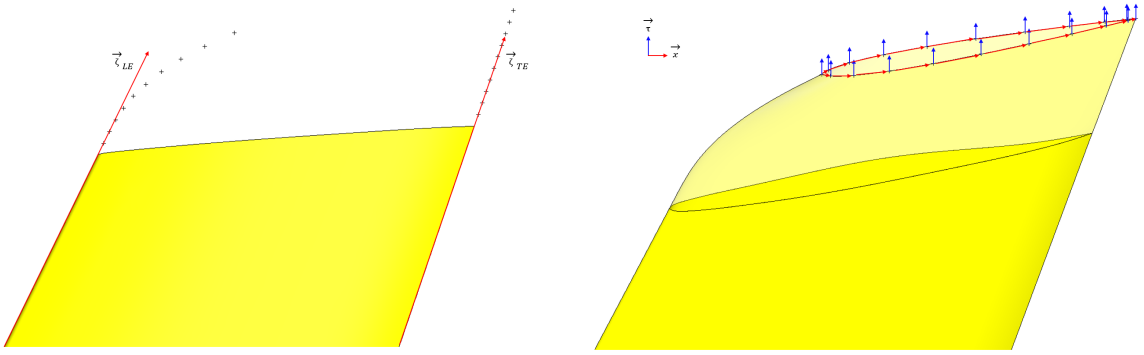

(a) Leading and Trailing Edge Definition for the Kuchemann Tip

(b) Definition of Semi-Elliptic Curves for the Rounded Wing Tip

Figure 3.4: Geometric Definition of the Curves Used to Parameterize the Wing Tip

In addition to reducing the strength of the wing tip vortices, rounded wing tips also help resolve convergence and stability issues in Euler and RANS analyses [45]. For these reasons, it was decided to add wing tip rounding as an additional parameterization constraint to the Kuchemann tip trunk design. The model presented by Galbraith et. al [45] was employed for this purpose. Semi-elliptical sections longitudinal to the winglet as shown in Figure 3.5a are generated from the Kuchemann tip airfoil coordinates, to produce a surface that is G1 continuous with the winglet. It must be noted that a NACA symmetric airfoil with a matching thickness to chord ratio to that of the winglet tip is used for the Kuchemann tip airfoil. The longitudinal semi-elliptic sections are defined by their centroids (Equation 3.3) and conjugate diameters (Equation 3.4 and Equation 3.5) at a particular chordwise location t.

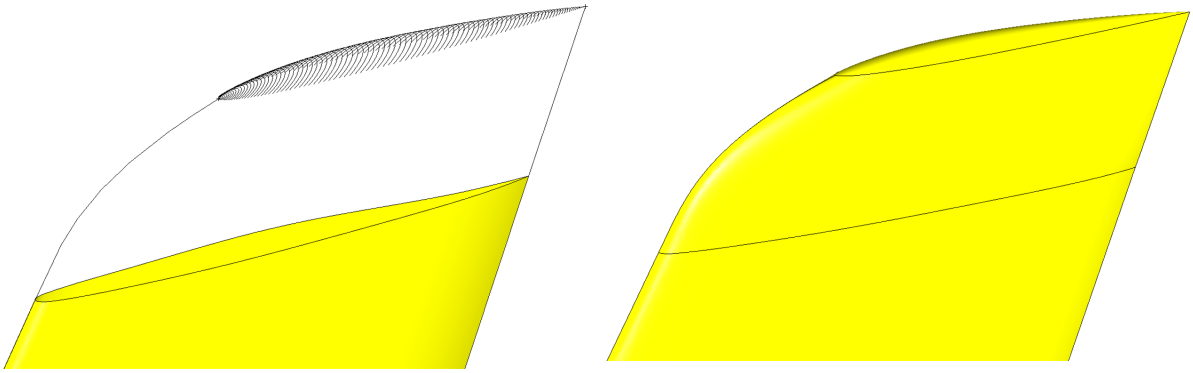

(a) Sections Used for Lofting

(b) Kuchemann Trunk and Rounded Tip Surfaces

Figure 3.5: ParaPy CAD Views of Parameterized Kuchemann Tip with a Rounded End

$$\vec{x_0} = \frac{1}{2} \cdot (\vec{x_U} + \vec{x_L}) \tag{3.3}$$

Where, $\vec{x_U}$ and $\vec{x_L}$ are the upper and lower Kuchemann tip airfoil coordinates, and $\vec{\tau_U}$ and $\vec{\tau_L}$ are the vectors tangent to the upper and lower Kuchemann tip trunk surfaces respectively. A visualization of these parameters in reference to the Kuchemann tip trunk is shown in Figure 3.4b. The parameter r controls the magnitude of the major conjugate diameter $\vec{d_2}$ and the shape of the semi-elliptical curve. Setting $r = 0$ produces a flat tip, while $r = 1$ produces a circular tip; And when $r > 1$, elliptical tips are generated.

$$\vec{d_1} = \frac{1}{2} \cdot (\vec{x_U} - \vec{x_L}) \tag{3.4}$$

$$\vec{d_2} = r \cdot \left|\vec{d_1}\right| \cdot \frac{\vec{\tau_U} \cdot (1-t) + t \cdot \vec{\tau_L}}{\left|\frac{1}{2} \cdot (\vec{\tau_U} + \vec{\tau_L})\right|} \tag{3.5}$$

Once the semi-elliptical sections are produced on the tip of the Kuchemann trunk, a B-spline surface is used to produce a rounded tip cap as seen in Figure 3.5b. The blend trunk, winglet trunk, Kuchemann tip trunk and the rounded wing tip cap are then used to produce a complete closed shell defined as the winglet shell.

3.1.3 Rudder Parameterization

A generic rudder model was parameterized by taking the updated winglet design as the drawing board. Since the purpose of the geometry was to be used in a RANS analysis the consideration of slots and gaps was essential to realistically quantify the effect they have on the rudder effectiveness and to make the spatial discretization process smoother. As seen on production aircraft, the streamwise slot or gap is maintained ensuring G1 continuity with the fore of the winglet section, while the lateral slots or gaps are maintained as is also the standard practice in many previous computational studies such as those by Natale et al. [42] and Streher et al. [43]. This also prevents mesh intersection issues between the deflected and undeflected surfaces and allows for prism layers to be constructed on these lateral faces. In addition, the rudder modelled for the Flying-V ensures a stable parameterization keeping in mind its potential use for an optimization routine, which requires robust automated CAD generation for analysis. The rudder was created such that its total span could only spread the winglet trunk. This was due to the limitation imposed by the Kuchemann tip design since it is added on top of the existing winglet trunk. If the rudder was cut out with the Kuchemann tip in place, the stability of a parameterized design would be lost and would require manual intervention while in use for an optimization process.

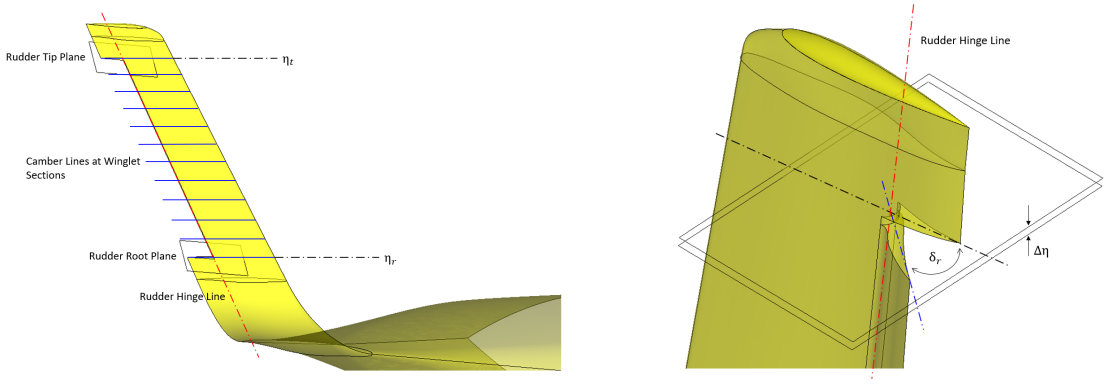

(a) Rudder Cutout Winglet with Hinge Line Definition

(b) Definition of Rudder Deflection and Lateral Gaps

Figure 3.6: ParaPy CAD Views of Parameterized Rudder

The rudder is modelled by first creating cutouts for the rudder as seen in Figure 3.6a. The cutouts are created by defining root and tip planes for the rudder, which are placed along the winglet span at respective root and tip spanwise fractions η_r and η_t. They are also moved along the chordwise direction to a particular chord fraction of the winglet at the corresponding spanwise locations. The airfoil shapes of the winglet at the rudder root and tip are used to create the rudder part. The airfoil coordinates are sorted to only include the coordinates aft of the chord fraction of the rudder at both the root and tip. The resulting cusp-shaped rudder airfoils at the root and tip are then lofted and attached to the cutout's edges as shown in Figure 3.6b.

G1 continuity between the rudder profiles and the cutout winglet profile is ensured by matching the tangent vectors at the intersection of these edges leading to a smooth surface even at large deflections as seen in Figure 3.7 which compares the cross-sectional shapes of the rudder sections on the winglet to that on the rudder-free zone. The rudder deflection's rotation is defined about the hinge line, which passes through the camber points of the local winglet airfoil section at the start and end of the rudder as evident in Figure 3.6a and Figure 3.6b. The lateral gaps are created by subtracting the cutout's span from a fraction $\Delta\eta$ larger than the rudder span at both the rudder root and tip. The lateral gaps are closed with a rounded finish to ensure a smoother transition at the trailing edge of the rudder cutout winglet trunk in the streamwise direction. This also ensures that the pressure gradient between the upper and lower winglet surfaces is minimal.

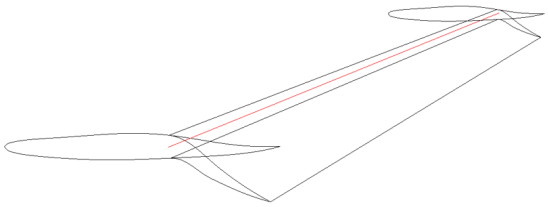

Figure 3.7: Airfoil Shapes with Rudder Deflected at -30 [°]

η_r [-]	η_t [-]	$(x/c)_r$ [-]	$(x/c)_t$ [-]	$\Delta\eta$ [-]	δ_r [°]
0.01	0.99	0.3	0.3	0.005	$\pm$ 30

Table 3.1: Rudder Design Parameters and Preliminary Values

The design parameters for the rudder are listed in Figure 3.1 with realistic baseline values for analysis. The span fractions for the rudder are at the limits of the winglet trunk to check the effect a full span rudder has on the stability and control derivatives. The chord fractions are limited to 30 % to account for the volume of the aft spar on the winglet. A study by Keller [46] displayed the ideal gap size for the rudder at extreme rudder deflections. A value for the gap size and a corresponding rudder deflection is used from this study, also taking into account realistic constraints that would be imposed on the maximum rudder deflection by the rudder actuator design and stick forces for the FV-1000. Additionally, the MMG was updated to produce differential deflection in the rudder, such that the mirrored component does not produce a symmetric rudder deflection but rather, the port and starboard side both are deflected in the same direction. The result of this is portrayed in Figure 3.8 for the FV-1000.

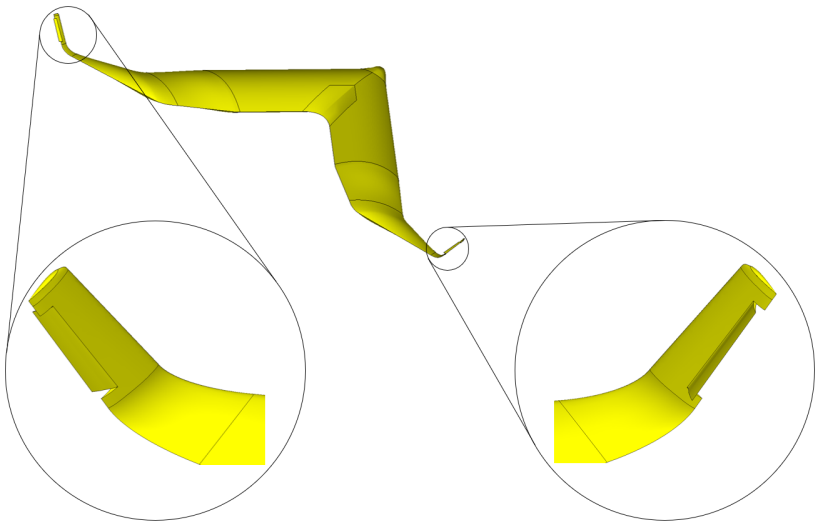

Figure 3.8: FV-1000 with Rudders Deflected at Defined Maximum of -30 [°]

3.2 Spatial Discretization and Flow Solver

The spatial discretization of the aircraft geometry was done using SALOME [2], an automated grid generation tool integrated into ParaPy, which allows the user to generate structured and unstructured meshes with various control and refinement options. For this study, a hybrid mesh consisting of triangle elements for the surface mesh, and tetrahedral elements with prism layers close to the wall for the volume mesh was used. An example of a coarse surface mesh that was generated for the FV-1000 with equally spaced triangle elements is displayed in Figure 3.9. The coarse mesh represents the baseline or minimum grid size used for a grid convergence study. The total thickness of the prism layers and the number of prism layers, with a defined growth ratio, was iteratively found in order to produce a Y+ distribution of less than 1 over the entire surface. The initial guess for the total prism layer thickness was derived from Reichardt's formula [47] for the boundary layer thickness over a fully turbulent flat plate Equation 3.6.

$$\delta = 0.37 \cdot \frac{x}{{Re_x}^{0.2}} \tag{3.6}$$

It was also found in the due process of analyzing the geometry in SU2 that some more modifications needed to be made to the flying-V geometry in order to make it feasible for an automated spatial discretization process. In particular, the length of the tapered trunk was reduced by 0.5 [m] and the leading edge distance of the toroidal trunk (distance between sections 1 and 2) was increased by 0.5 [m]. The Whitcomb airfoils used for the outer wing tip entail a highly cusped trailing edge, which necessitated a large number of surface mesh cells to ensure a good quality aspect ratio and skewness cells in the surrounding region. The order of mesh refinement to meet these criteria was deemed too high to meet the optimization grid size requirements. Therefore, an alternative was to reduce the cusp by reducing the magnitude of the CST coefficients that controlled the trailing edge definition. This also implies that there is some influence of the airfoil shape on the airfoil optimization design space, in that, airfoil shapes with a strong trailing edge cusp maybe be filtered out by the optimizer due to a diverging solution if not a failed meshing attempt. The meshing process also defines the boundary conditions used for the RANS analyses. The freestream boundary condition is used for the far-field and the no-slip wall boundary condition is used for the aircraft. Due to the whole aircraft being used for the RANS analysis, the benefit of the symmetry boundary condition is lost.

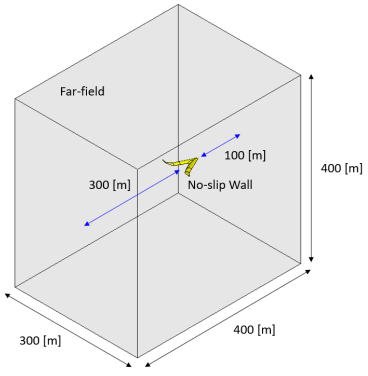

(a) Boundary Conditions Imposed on the Flow Field During the RANS Analyses

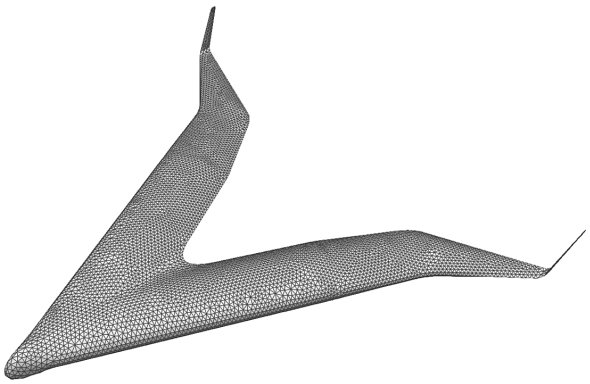

(b) An example of a Coarse Surface Mesh on the FV-1000

Figure 3.9: Elements of the Spatial Discretization Process

The Stanford University Unstructured (SU2) [48] computational analysis and optimization tool was used

[2]SALOME. *SALOME Platform Documentation*. Retrieved 23 March, 2023 from `https://docs.salome-latform.org/7/gui/SMESH/index.html`

for the RANS analysis. It is a computationally efficient solver due to the lack of complex user interfaces, and its focus includes optimization functionalities which made it an attractive choice for use in this research. SU2 offers various turbulence models that can be used to simulate the turbulent flow of fluids. The most commonly used turbulence models in SU2 are the Spalart-Allmaras (SA), k-epsilon, and k-omega models [48]. The Spalart-Allmaras model is a one-equation model that is widely used for aerospace applications. It solves a transport equation for a turbulent viscosity variable and has been shown to provide accurate results for attached and separated flows [49]. Due to these reasons, the SA model was opted for during the optimization and analysis runs. The SA model is also relatively stable and has been successfully used by past researchers like Faggiano [7], and Brouwer [39], resulting in successful optimizations for the Flying-V. With relation to the subject of the convective schemes used by the flow solver, SU2 [48] provides many central and upwind schemes for compressible and incompressible flows. Central schemes like the Jameson-Schmidt-Turkel (JST) [50] are generally less dissipative and are a more stable option but suffer from high grid dependency to produce accurate solutions [48]. Upwind schemes on the other hand can produce more accurate solutions but often require slope limiters and higher relaxation factors to limit oscillatory and/or non-physical solutions especially where shock discontinuities may be present. For these reasons, the JST convective scheme with second and fourth-order coefficients for the scalar dissipation is used [50]. In the context of optimization, these coefficients allow for a more adaptive solution technique that partially removes grid dependency. If the grid leads to a diverging solution, these coefficients can be tweaked to force the solution to converge.

3.3 Sensitivity Analysis

An analysis was done to study the sensitivities of the winglet design parameters to the objectives defined. Instead of the classical one-at-a-time (OAT) approach the elementary effects (EE) or Morris method was used [51]. This method is comparable to the OAT in that it adheres to the concept of local variation around a base point, but improves upon it. The local variation is done to the proceeding design variable in the design set until the final parameter, leading to what is called trajectories (Figure 3.10a). The advantage is that this averages a number of local measures so as to remove the dependence on a single sample point and can prevent the problem of cancellation effects, where one variable may have an effect that is coupled to the value of another.

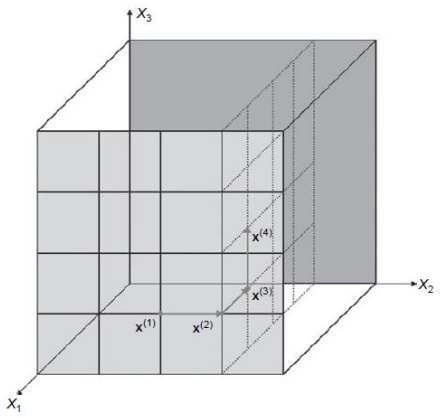

(a) An Example of Trajectories from Saltelli et al. [51]

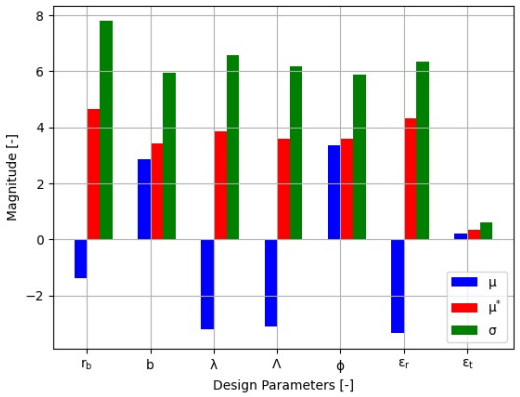

(b) Winglet Design Parameter Sensitivity Measures

Figure 3.10: Sensitivity Analysis - Elementary Effects

For the current study, 8 trajectories were defined as the sample space and the analysis was done through the python implementation of this method in SALib library [3]. The sampling that resulted from this was also used

[3]SALib. *Sensitivity Analysis Library in Python* Retrieved 23 March, 2023 from `https://salib.readthedocs.io/en/latest/`

to identify errors arising from geometry generation, spatial discretization and solution processes. The patterns in the errors were used to make the optimization framework more robust by implementing strategies to resolve them. This is explained in the following section. The results of the sampling study led to the generation of a sample of 66 winglet designs, from which a baseline design for the optimization process that was feasible from an aerodynamic efficiency perspective was picked, with the motivation of reducing the winglet trunk span. The sensitivity analysis results are presented in Figure 3.10b. The standard deviation σ defines the dependency of a parameter's effect on the others, and it can be seen that besides the winglet tip twist angle, all the other parameters have a strong influence on each other. The mean of the objectives of a parameter μ defines its influence on the objective, while the absolute mean μ_* indicates the directions the effect of the parameter can take. If the conjugate means both have a large magnitude, it implies that the parameter always has the same effect. If the value of μ_* is high but that of μ is low, it implies that the parameter has varying effects. All winglet platform parameters display differing values for the magnitudes of the conjugate means, implying that they have varying effects. But these effects vary in their degree as can be seen when comparing the pair of values for the blend radius, which has the lowest value of μ, to that of the cant angle. This is also validated by the fact that it has the highest value of σ. The sensitivity parameters are calculated using Equation 3.7, Equation 3.8 and Equation 3.9.

$$\mu_i = \frac{1}{r} \cdot \sum_{j=1}^{r} E_i^j \tag{3.7}$$

$$\mu_i^* = \frac{1}{r} \cdot \sum_{j=1}^{r} \left| E_i^j \right| \tag{3.8}$$

$$\sigma_i^2 = \frac{1}{r-1} \cdot \sum_{j=1}^{r} (E_i^j - \mu)^2 \tag{3.9}$$

Where,

$$E_i^j = \frac{f(x_i^j + \Delta x_i^j)}{\Delta x_i^j} \tag{3.10}$$

And, $i = 1, ..., k$ and $x^i \in \boldsymbol{X}^j$. Subsequently, $j = 1, ..., r$ and $\boldsymbol{X}^j \in \boldsymbol{\Pi}$

The value E determines the (elementary) effect of a design variable i in a particular trajectory j, from the set of trajectories used in the sampling r. The reader is forwarded to the works of Saltelli et al. [51] for a more detailed account of this approach.

Step	r_b [m]	b [m]	λ [-]	Λ [°]	ϕ [°]	$\boldsymbol{\epsilon}$ [°]	$\boldsymbol{A}_r$ [-]	$\boldsymbol{A}_t$ [-]
1	[2.5, 0.3]	[10, 2]	[1, 0.3]	[50, 0]	[50, 0]	[15, -15]	-	-
2	[2, 0.5]	[6, 3]	[0.75, 0.35]	[45, 30]	[35, 10]	[10, -10]	-	-
3	-	-	-	-	-	[10, -10]	[200%, 50%]	[200%, 50%]

Table 3.2: Bounds Used for the Winglet Design Variables During Different Optimization Steps

The sensitivity analysis was also used to determine the extent of the values for the winglet's design parameters. The bounds used are progressively refined for the optimization steps. These are shown in Table 3.2, where step number 1 indicates the sensitivity analysis, 2, is the planform optimization, and 3, is the airfoil optimization.

3.4 Optimization Setup

The RANS method chosen for the optimization process poses a relatively large computational time to obtain a solution. Coupled with the fact that the winglet design is parameterized by 31 design variables, which can lead to excessively large wall times, the optimization process was split into two steps. The planform is first optimized, and the solution from this step is used in the airfoil optimization. Due to the lack of readily available data for stability derivatives that can ensure a statically stable aircraft, and the fact that the unconventionality of the Flying-V limits the usage of data frequently used for conventional aircraft, stability was considered as an equally weighted objective of the optimization rather than a constraint. The dynamic yawing moment due to sideslip $C_{n_{\beta_{dyn}}}$ defined in Equation 3.11, was considered as the objective to maximize the lateral-directional stability. The value of $C_{n_{\beta_{dyn}}}$ dictates the undamped natural frequency of directional divergence and the Dutch Roll mode, and the correlation was demonstrated by Greer [52] through wind tunnel and flight tests, specifically for highly swept wings at high angles of attack.

$$C_{n_{\beta_{dyn}}} = C_{n_\beta} \cdot \cos\alpha \cdot - \left(\frac{I_z}{I_x} \cdot C_{l_\beta} \cdot \sin\alpha\right) \tag{3.11}$$

The aerodynamic optimization is performed at cruise while the stability optimization is performed at approach conditions. Sideslip angles that represent the maximum cross-wind operational bounds were used to evaluate the slope of the stability curves. CS25.177(c) by the European Union Aviation Safety Agency (EASA) [13] specifies a method to evaluate the maximum sideslip angle experienced by the aircraft in a steady, straight sideslip during crosswind landing and take-offs. This method is given by Equation 3.12. Using this, the maximum sideslip angle experienced by the FV-1000, given its approach speed leads to a value of 15 [°]. This value of 15 [°] also matches the value stated by [13]: "Experience has also shown that a maximum sideslip angle of 15 degrees is generally appropriate for most transport category aeroplanes even though the equation may provide a higher sideslip angle", and hence is considered a relevant design point to evaluate the stability objective functions.

$$\beta = \arcsin(\frac{36}{V}) \tag{3.12}$$

This ultimately leads to three RANS analyses for a single function evaluation. It is assumed that these polars are linear in nature between these sideslip angle extremes even though this is not the case as will be explained in the following sections. The definition of the design points of the optimization process is shown in Table 3.3. The multi-objective planform optimization problem can then be defined as follows.

$$\begin{aligned}
&\underset{\boldsymbol{X}}{\text{minimize}} && f(\boldsymbol{X}) = \left(\frac{j_{1_{ref}}}{j_1}\right) \cdot w + \left(\frac{j_{2_{ref}}}{j_2}\right) \cdot (1-w) + g(\boldsymbol{X}) \\
&\text{subject to} && \boldsymbol{X}_L^i \leq \boldsymbol{X}^i \leq \boldsymbol{X}_U^i \text{for i} = 1,...,7 \\
&\text{where} && \boldsymbol{X} = [b, r_b, \lambda, \Lambda, \phi, \epsilon_r, \epsilon_t] \\
& && j_1 = \frac{C_L}{C_D} \quad \text{and} \quad j_2 = C_{n_{\beta_{dyn}}} \\
& && g(\boldsymbol{X}) = \left|\frac{C_L}{C_{L_{des}}} - 1\right| \cdot p
\end{aligned}$$

In the interest of a less expensive optimization run time for the airfoil optimization process, due to the number of design variables, the airfoil optimization was performed only at cruise, with a single objective and 12 CSTs each for the root and tip winglet airfoils. An assumption was made that the airfoil shapes do not greatly affect the stability objectives of the winglet. The twist angles were again included in this step to allow enough flexibility for the optimizer to target an ideal elliptic lift distribution. Distance-based penalties as described by Smith et al. [53], typical of those used for gradient-free optimization processes are used to

Point	C_L [-]	α [°]	β [°]	M [-]	H [m]	Re $(\cdot e^7)$ [-]	CG [% $\bar{c}_a$]	
Cruise	0.3	-	-	0.85	13000	8.54	25	-
Approach	-	18	15, -15	0.22	0	9.34	15	

Table 3.3: Design Point Operating Conditions and Reference Values

ensure that the target lift coefficient is met at cruise for both the optimization steps. The parameter p was used to scale the intensity of the penalty depending on the magnitude of the constraints violated. Structural thickness constraints in the form of maximum airfoil thickness-to-chord ratios were also enforced with the same distance-based penalties during the optimization process. It must be mentioned that the initial thickness constraints for the airfoils were violated as a result of the values used from previous studies. A target maximum thickness of 10% is enforced for both airfoils. The airfoil optimization problem is defined below.

$$
\begin{aligned}
\underset{\boldsymbol{X}}{\text{minimize}} \quad & f(\boldsymbol{X}) = \left(\frac{j_{ref}}{j}\right) + \sum_{i=1}^{3} g_i(\boldsymbol{X}) \\
\text{subject to} \quad & \boldsymbol{X}_L^i \leq \boldsymbol{X}^i \leq \boldsymbol{X}_U^i \text{for i} = 1,...,26 \\
\text{where} \quad & \boldsymbol{X} = [\boldsymbol{A}_{r_u}, \boldsymbol{A}_{r_l}, \boldsymbol{A}_{t_u}, \boldsymbol{A}_{t_l}, \epsilon_r, \epsilon_t] \\
& j = \frac{C_L}{C_D} \\
& g_1(\boldsymbol{X}) = \left|\frac{C_L}{C_{L_{des}}} - 1\right| \cdot p \\
& g_2(\boldsymbol{X}) = \left|\frac{(t/c)_r}{(t/c)_{r_{ref}}} - 1\right| \cdot p \\
& g_3(\boldsymbol{X}) = \left|\frac{(t/c)_t}{(t/c)_{t_{ref}}} - 1\right| \cdot p
\end{aligned}
$$

The differential evolution (DE) algorithm defined by Storn et al. [54] was used in performing both optimization steps. The python application programming interface was used in the implementation of the optimization processes [4]. The DE algorithm is a gradient-free evolutionary-based algorithm, that is capable of finding the global optimum for a given optimization problem. It allows for the parallelization of the objective function evaluation for multiple designs simultaneously which makes it attractive for run time expensive analysis methods such as RANS used in this reasearch. For the current optimization problem, the 'currenttobest1bin' mutation strategy was used, as it offers the best diversity for a given sample set as suggested by Storn et al. [54]. Mutation constants in the range [0.2, 1.8] were used to maximize the winglet design space the optimizer could search from the specified bounds for each of the design variables. A recombination value, which specifies the portion of the population from the previous generation to be used to evaluate the next population, 0.6 is used. A balance between the mutation and recombination values was achieved by iteratively checking the extent of the sample space the optimizer would produce for each succeeding population before the optimization with RANS was actually done. All the samplings were generated using the Latin hypercube sampling (LHS) method. The DE algorithm uses a standard deviation-based convergence criterion, where if the standard deviation of the objective function for the current population is lesser than the standard deviation for the previous population by a given tolerance, the solution is converged. No convergence was achieved during the planform optimization step likely due to the smaller population sizes used. The planform optimization process was run for 8 generations with a population size of 21 each, while the airfoil optimization step

[4] SciPy. *Differential Evolution* Retrieved 23 March, 2023 from `https://docs.scipy.org/doc/scipy/reference/generated/scipy.optimize.differential_evolution.html`

was run for 15 generations with a population size of 24 each. The differences in the number of generations evaluated are attributed to the time a function evaluation takes during each optimization step. Due to this, the best-performing candidate is picked from the final generation as the optimum of the planform optimization step. The flow of the optimization processes is better explained in the flowchart presented in Figure 3.11, which explains the different steps taken and the resulting winglet designs from these processes.

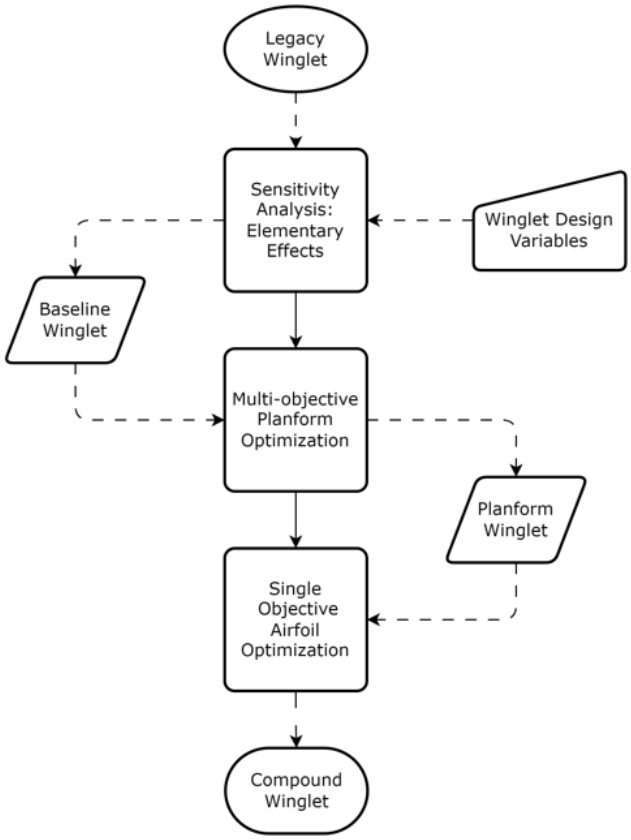

Figure 3.11: Winglet Optimization Process Flow

The optimization framework that was built is described with its elements and the process flow in detail in Figure 3.12. The optimization is started by connecting to a workstation that is capable of handling multiple processes to enable parallelization and enough memory to contain the grid data that are generated for the different designs. The DE algorithm makes use of the multiprocessing library within python to allow running multiple objective function evaluation processes in parallel [5]. The specified number of processes are started by the DE algorithm and individual sets of winglet design parameters are fed to each one from the current population. The process of generating the geometry and the volume grid for the analysis is then initiated for all these designs. Once a successful geometry and grid are generated for a given case, the case data is packaged and uploaded onto the High-performance computing (HPC) facilities, where a particular cluster node is deployed to run the solution on a localized version of SU2. Once the solution is obtained, the case data is packaged and downloaded back onto the workstation, where the values of the corresponding penalties and objective functions are then processed and fed back to the optimizer. An adaptive mesh or solution generation technique is used, by matching the issue or bug that may occur during these processes to the issues that were identified during the sampling study in the sensitivity analysis, and a fixed number of attempts are made to solve each issue. If the attempts fail at fixing the issue, penalties are added to completely eliminate or punish design points that are not able to either generate geometry, grid or solution data.

[5]Python. *multiprocessing — Process-based parallelism* Retrieved 23 March, 2023 from `https://docs.python.org/3/library/multiprocessing.html`

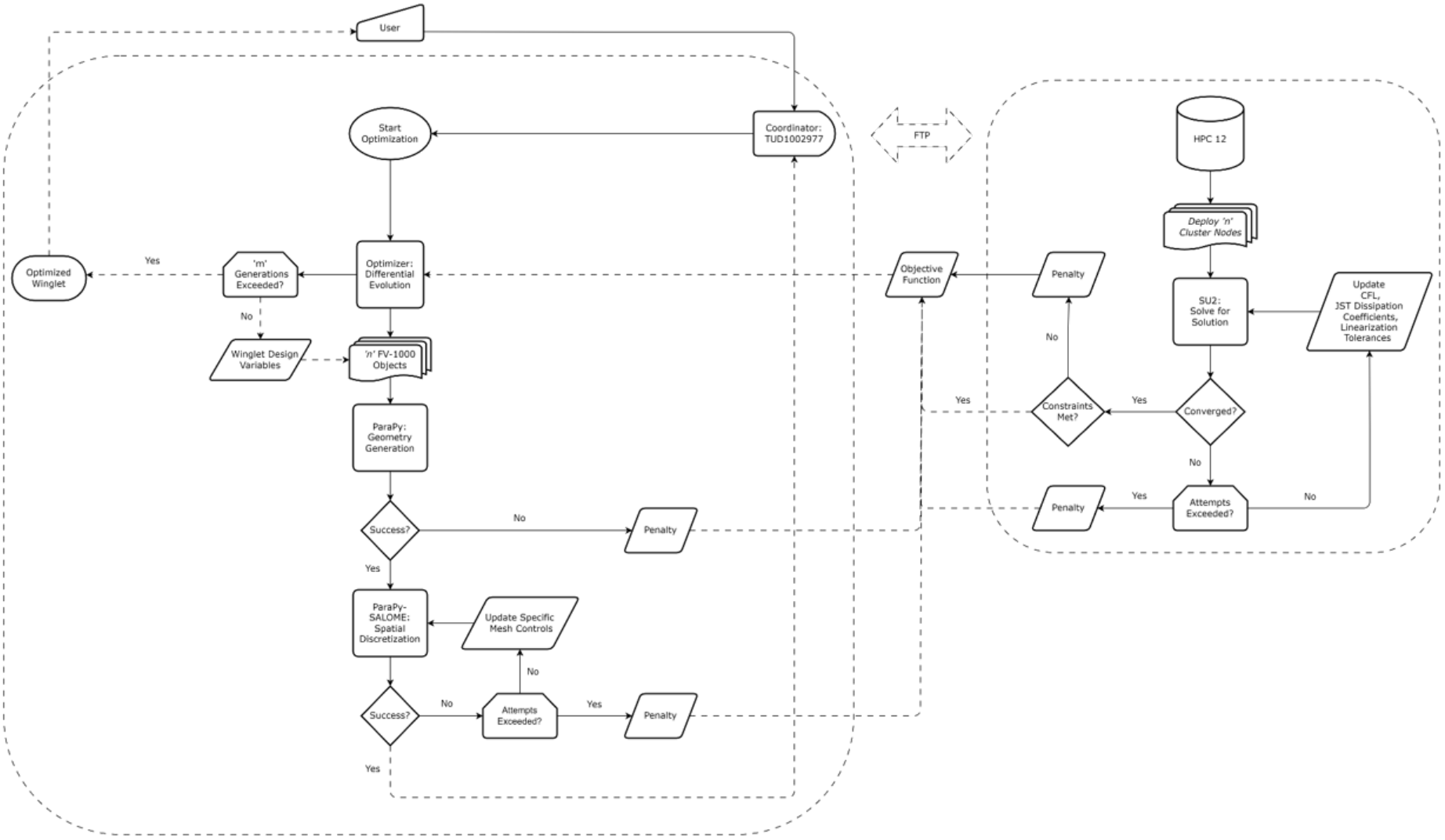

Figure 3.12: Winglet Optimization Framework Setup

Chapter 4

Validation and Verification

This section elaborates on the validation and verification studies performed for the aerodynamic analysis method used in this study.

4.1 ONERA M-6

A quick validation and verification study is performed with a case that is representative of the geometry and operating conditions of the analysis and optimization process. The ONERA-M6 [1] is one of the most widely tested and accepted benchmark cases used for validation. The validation is performed against the wind tunnel experiment conducted by Schmitt et al. [55]. A 12 million cell count grid is used to conduct the validation, which also represents the maximum and finest grid level used in the analysis of the FV-1000 during a grid sensitivity that will be explained further in section 4.2. From the pressure distributions in Figure 4.1 for the wing root, Figure 4.2 for the midsection of the wing and Figure 4.3 for the wing tip, it can be seen that SU2 predicts the magnitude of the suction peaks throughout the wing accurately, however at slightly aft chordwise locations.

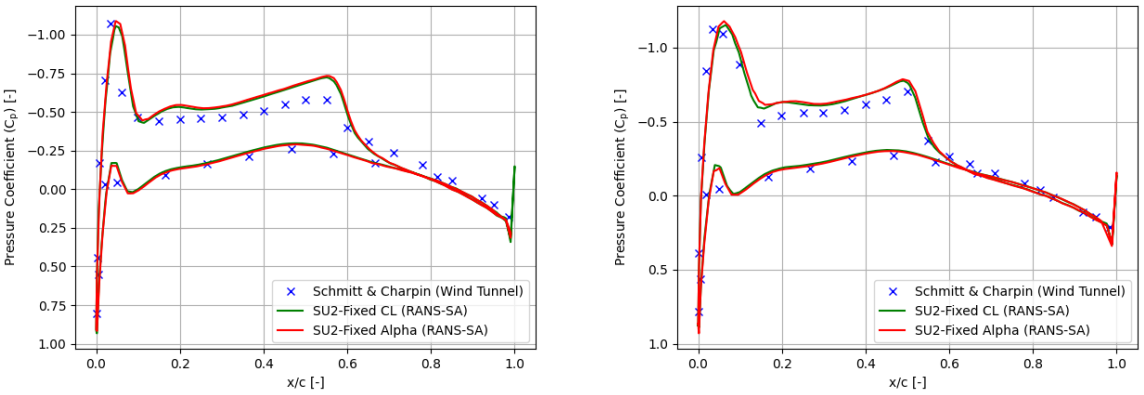

(a) η_{20} (b) η_{44}

Figure 4.1: Validation of Pressure Coefficient Distributions from SU2 for the ONERA M6 Wing Root

The location of the shock is predicted accurately at the wing root and tip as shown in Figure 4.1 and Figure 4.3, but the magnitude of the supervelocities are overpredicted at the root at η_{20} and η_{44}, while at the tip the shock strengths match that of the experiment in both fixed angle of attack and lift modes. In the

[1] ONERA-M6 Wing. Retrieved 23 March, 2023 from `https://www.grc.nasa.gov/www/wind/valid/m6wing/m6wing.html`

midsection of the wing at η_{65} and η_{80}, the transition from the suction peaks to the shock sitting at chordwise locations of 30 % and 20 % is not captured by either of the two modes. While the experiment shows a strong shock-induced separation due to the adverse pressure gradient leading up from the suction peak, SU2 predicts a more gradual pressure relief at η_{65} and η_{80} as seen in Figure 4.2a and Figure 4.2b. The mid-wing section is also where the differences between the two modes are the most distinct.

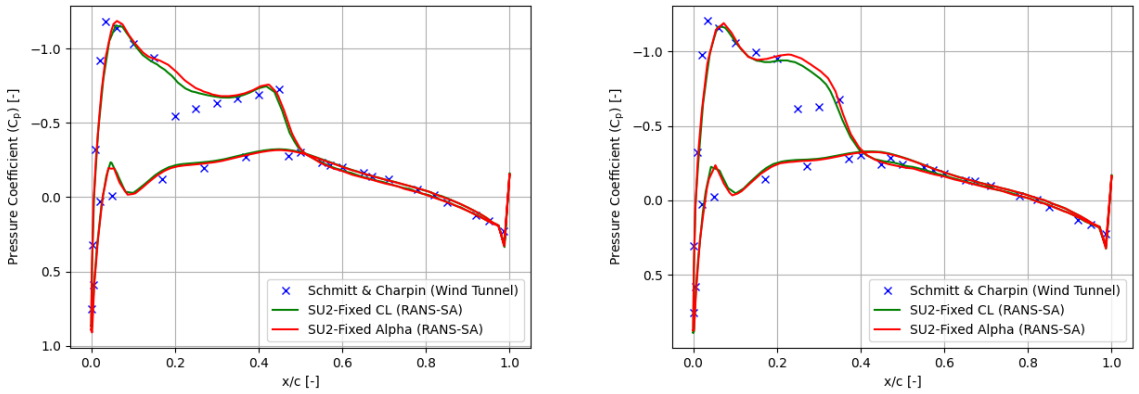

(a) η_{65} (b) η_{80}

Figure 4.2: Validation of Pressure Coefficient Distributions from SU2 for the ONERA M6 Mid-wing

While the fixed lift mode is closer to the experiment, it is possible that this is due to the bias that is inherent due to the lift value being set as the target. While at the operating lift, the pressure distribution may seem a little more accurate than the fixed lift mode, we see from Table 4.1 that the angle at which it achieves this is a lot lower. It can then be said that SU2 in general overpredicts the lift due to the fact that if the angle of attack is increased, the lift over the wing is again overpredicted as is the case with the fixed angle of attack mode seen in the pressure distributions and Table 4.1. The predictions over the pressure sides are more accurate at the root and mid-wing section compared to the tip, where local separation bubbles are not seen by the computational solver at the wing tip at any spanwise locations (Figure 4.3).

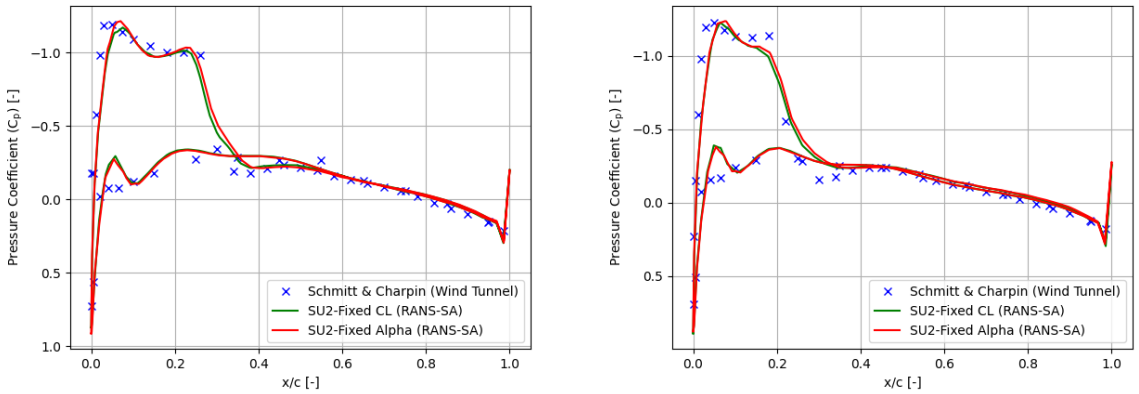

(a) η_{90} (b) η_{95}

Figure 4.3: Validation of Pressure Coefficient Distributions from SU2 for the ONERA M6 Wing Tip

A comment must also be made about the sudden spikes seen at the trailing edges in all the pressure distributions. It is found after plotting the $Y+$ distribution over the wing that the value for the $Y+$ spikes up close to the trailing edge. Although the values are still below 1, the relative difference with the rest of the wing

is significant, causing the sudden spike in the pressures. This issue is correlated to the quality of the mesh at the trailing edge. As was mentioned in section 3.2, the sharp trailing edge causes the prism layer transition from the suction to the pressure side to be highly skewed. This leads to the inaccurate solution observed and is also found in some grid sizes to cause oscillatory behaviour in the residuals.

Mode	C_L [-]	α [°]	C_{D_p} [counts]	C_{D_f} [counts]	C_D [counts]	L/D [-]
Schmitt et al. [55]	-	3.06	-	-	-	-
Durrani et al. RANS-SA [56]	0.26	3.06	-	-	197	13.09
SU2 Fixed α RANS-SA	0.27	3.06	171	29.15	201	13.46
SU2 Fixed C_L RANS-SA	0.26	2.90	159	29.18	189	13.52

Table 4.1: Validation and Verification of Aerodynamic Coefficients from SU2 for the ONERA M6 Wing

To compare the two modes of SU2, the verification of the fixed angle of attack and fixed lift coefficient mode are performed against the numerical study by Durrani et al. [56]. The fixed lift mode uses the lift value from the literature to solve for the drag. From Table 4.1, it is seen that SU2 over-predicts both lift and drag compared to the literature in the fixed angle of attack setting. The over-prediction can be correlated to the over-prediction of the suction seen in the pressure distributions closer to the wing root. From this tendency, one should expect that the fixed lift mode predicts the same lift coefficient at a smaller angle of attack since the fixed CL mode is an extension of the fixed angle of attack mode. This is confirmed by the values that are obtained in the fixed CL mode, which also portrays small underpredictions in the pressures as seen in the plots above.

4.2 Grid Sensitivity Study

A grid sensitivity study was conducted by varying the number of surface and volume mesh elements and studying their effect on the accuracy of the solution. The coarse level mesh that was defined in section 3.2 was scaled up to medium and fine grid levels in multiple steps in order to analyse the sensitivity. A complexity a multi-objective and multi-point optimization study introduces is the large number of output variables that are to be obtained at different conditions. In addition, the optimization process itself imposes requirements such as run times and sufficient sensitivity to the solution for a given grid size. Taking all these aspects into account, the grid sensitivity study was not limited just to the cruise point, but also the approach conditions, where the stability coefficients are obtained. The sensitivity of the grid is also not limited just to the lift and drag but also the force and moment coefficients along the various wind axes. The errors in the force and moment coefficients are measured as a percentage with respect to the finest grids tested in each case, that being 12 million mesh elements. This mesh count was validated in the previous section with a benchmark case, providing more confidence to the solutions that are obtained for the aircraft using this mesh. The errors are calculated using Equation 4.1 where C represents a particular force or moment coefficient at a particular grid level C_i, and at the finest grid C_{fine}.

$$\epsilon = \frac{C_i - C_{fine}}{C_{fine}} \cdot 100 \tag{4.1}$$

The results of this study are depicted in Figure 4.4 and Figure 4.5. It can be seen in Figure 4.4a that the drag errors at a fixed lift coefficient at cruise converge quite well going to a margin of less than 5 % already at 6 million volume elements. The lift coefficient errors at an approach angle of attack of 18 [°] shown in Figure 4.4b display an oscillatory behaviour going to higher cell counts but seems to be damped going further

closer to 12 million cells. The lift coefficient errors also converge to a margin of less than 1 % as early as 4 million volume cells.

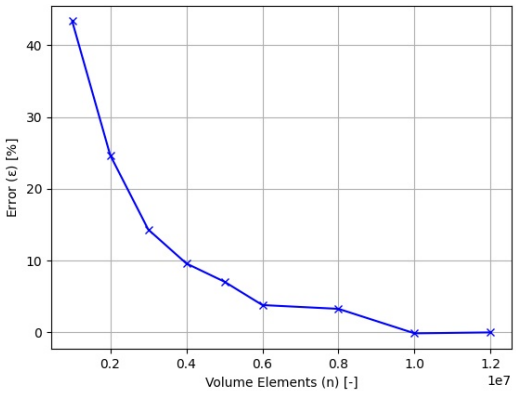

(a) Discretization Errors of Drag at Cruise

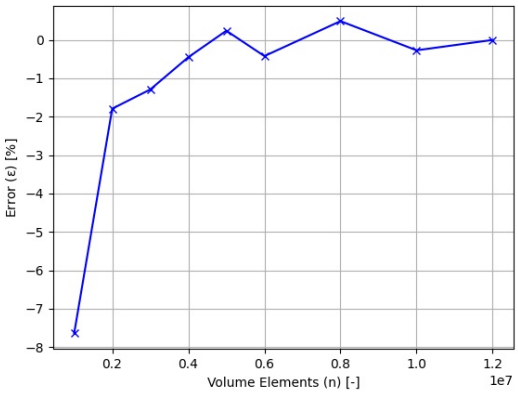

(b) Discretization Errors of Lift at Approach

Figure 4.4: Effect of Increasing Grid Sizes on Lift and Drag Coefficients

The side force, yawing and rolling moment coefficients at approach does not display an asymptotic behaviour in their convergence as shown in Figure 4.5a. The yawing moment coefficient and the side force coefficient exhibit similar behaviours in their convergence but produce a steep descent towards the 12 million cell count. While the rolling moment coefficient is seen to start producing a steadily decreasing value, trying to produce an asymptotic nature, the limit of the 12 million cell count limits the complete picture. Due to the limitations imposed on the computational resources that further limits getting a complete picture of the convergence of the stability coefficients, it is assumed that the convergence of these variables possibly occurs at even higher grid sizes. For the current study, the implication of this is that the solutions of the optimized designs being compared at the end have a lower confidence level compared to the lift and drag coefficients as to the actual nature of the solutions. Lastly, the elapsed time taken by each grid to produce a solution as shown in Figure 4.5b, is also considered for both operating points, as this played a fundamental role in the run times of the optimization process.

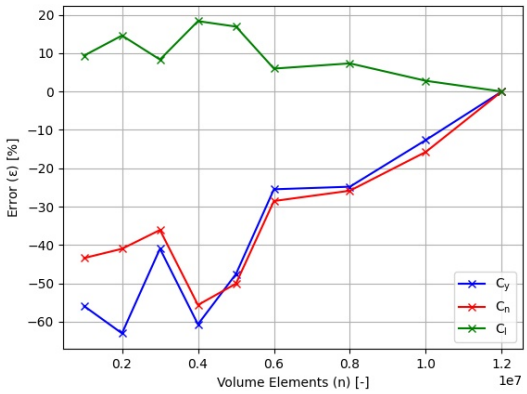

(a) Discretization Errors of Side Force, Yawing and Rolling Moment Coefficients at Approach

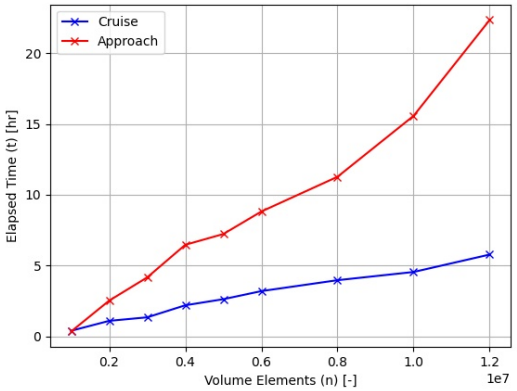

(b) Solution Times at Design Points

Figure 4.5: Effect of Increasing Grid Sizes on Stability Coefficients and Solution Time

It can be seen that the solution times are more critical for the approach simulations than the fixed lift cruise simulations. This is a severely limiting factor in the optimization study as in addition to the higher run

times, the number of simulations that need to be run in order to obtain the objectives is higher. This then also limits the number of runs that can be performed in order to obtain the stability coefficients, as was taken into account while planning the optimization setup in section 3.4. Taking these parameters into account, it was decided to use a grid size of 5 million volume elements for the optimization process as this provided a good balance of accuracy and solution time.

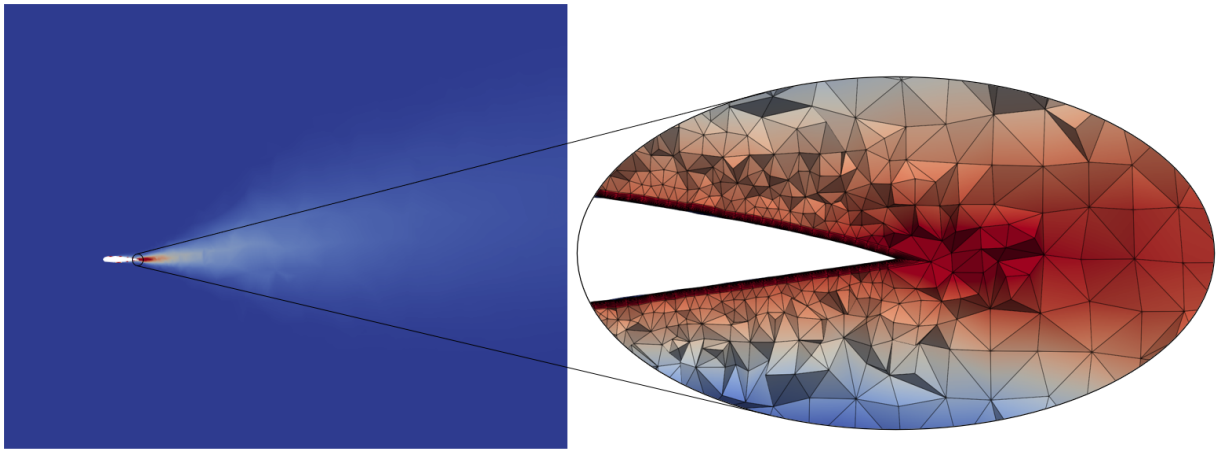

Figure 4.6: Verification of Domain Size and Prism Layer Height Through Eddy Viscosity Contours

A comment must be made on the boundary layer resolution of the grid and the size of the domain selected while running the RANS analyses. The resulting grid used for all RANS analyses consisted of 50 prism layers with a growth ratio of 1.2, with an overall thickness of 18 [cm]. The iterative approach that was mentioned in section 3.2 for the boundary layer size approximation was verified by looking at the eddy viscosity contours over the aircraft as they shed light on the intensity of the turbulence in the flow field and magnify the boundary layer development over walls. This is plotted in Figure 4.6 where it is seen that the prism layers encompass most of the boundary layer until the trailing edge wake, where the boundary layer grows significantly and the prism layer thickness is not sufficient anymore. This is to be expected as the boundary layer has a varying thickness along the wall. This is even more severe when considering the fact that the approach phase has a thicker boundary layer and requires a much larger prism layer definition to be able to capture the wake. But as this would lead to a new routine to generate a mesh disparate for the cruise and approach phases, leading to longer optimization run times, it was decided to use the same mesh for both design points.

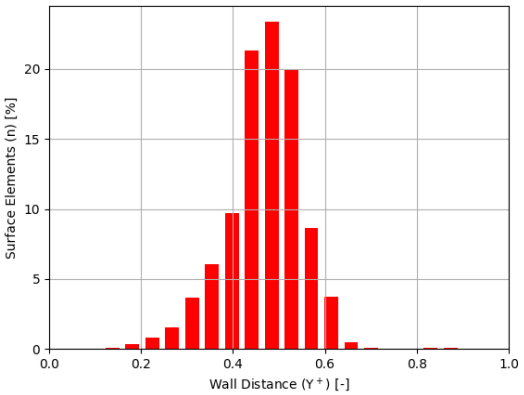

Figure 4.7: Wall $Y+$ Distribution over the Aircraft Surface

Domain Size (x, y, z) [m]	ϵ_L [%]	ϵ_D [%]
(300, 200, 300)	1.81	2.14
(400, 300, 400)	0.92	1.03
(500, 400, 500)	0.67	0.86

Table 4.2: Sensitivity of Lift and Drag Coefficient Errors to Far-field Size

The resulting $Y+$ distribution over the grid for the optimization mesh is shown in Figure 4.7 and represents

a standard bell curve distribution as is expected. It can be seen that all the elements have a $Y+$ value of less than 1. In the previous section, it was noticed that there was a sudden spike in the pressure distribution which was attributed to the $Y+$ distribution of the cells. This is confirmed here, seeing that there are some cells that have a relatively high $Y+$ value compared to the rest of the elements. A sensitivity study to the domain size also was performed as shown in Figure 4.2. It is seen that the sensitivity is relatively low for both the lift and drag when again compared to the largest domain. The eddy viscosity contours plotted in Figure 4.6 also show their values over the entire domain. Here it is seen that the wake behind the aircraft subsides going closer to the aftmost far-field boundary. It can be concluded that the domain size is large enough to effectively resolve the wake behind the aircraft and no wall-bounded reflections are found which could have affected the solution accuracy.

4.3 Solution Benchmarking

Analyzing some initial results for the stability coefficients revealed an anomaly in the behaviour of the side force and yawing moment coefficients for different cases. At zero sideslip angles, the polars do not pass through the origin as shown in Figure 4.8a and Figure 4.8b, implying that the aircraft geometry was not symmetric. Since the Flying-V aircraft geometry is mirrored from a half geometry, this possibility as the potential problem was eliminated. The only other source this could potentially occur from was the spatial discretization process. To narrow down on the source of error, the baseline polars for the Flying-V aircraft were rerun in an alternative industry-standard computational fluid dynamics (CFD) suite such as STARCCM+ with identical grid and solver settings. The meshing for the STARCCM+ case was done within the suite also using triangles, tetrahedrons, and prism layers. Comparing the solution from STARCCM+ to that of SU2 confirms the hypothesis that the source of error was indeed the spatial discretization process. The polars generated by STARCCM+ are symmetric and do not generate any side force or yawing moments at zero sideslip.

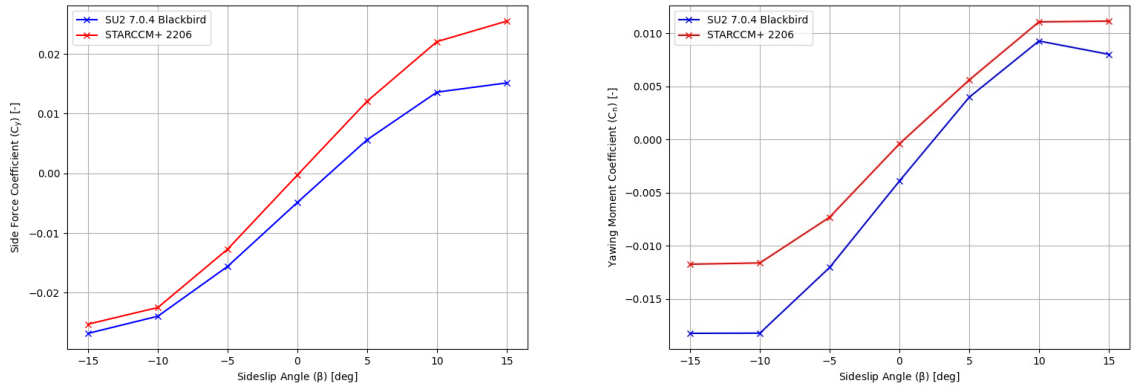

(a) Side Force Coefficient

(b) Yawing Moment Coefficient

Figure 4.8: Comparison of Sideslip Polars for Stability Coefficients of Different CFD Solvers

Chapter 5

Results

The results of the winglet analysis and optimization are presented in this chapter. The performance of the winglets at different optimization steps is broken down through a comparison of their aerodynamic and stability coefficients, along with an investigation of their polars to assess their off-design performance and the optimization's effect on it. In the succeeding sections, the flow features for the various winglets are examined at the cruise and approach conditions and an attempt is made to correlate physical phenomenon to the cumulated forces and moments seen in the aerodynamic and stability polars.

5.1 Design and Off-design Point Analysis

The winglet designs are labelled as the optimization steps proceed but are different from what the optimization processes are called since some steps incorporated the changes made in the previous steps. The initial winglet design used for the analysis in setting up the optimization processes is called the legacy design and is the design used by Cappuyns [12] and Luijk [40] in their analysis. The baseline design obtained from the elementary effects sensitivity analysis, and the planform-optimized design, are labelled as their processes suggest. Finally, the airfoil optimization step incorporated the planform-optimized design as the baseline for its optimization and hence is called the compound design. The aerodynamic and lateral-directional stability RANS assessment of the Flying-V aircraft without the winglets, defined here as the winglet-off case, was also performed for aerodynamic bookkeeping and comparison with the different winglet designs. The proceeding results are described by figures and tables utilising the above-defined nomenclature.

Design	C_L [-]	α [°]	C_{D_p} [counts]	C_{D_f} [counts]	C_D [counts]	L/D [-]	x_p [m]	S_w [m^2]
Winglet-off	0.30	8.36	421	38.83	460	6.52	22.19	1962.50
Legacy	0.30	8.51	435	38.78	474	6.33	21.90	1965.66
Baseline	0.30	8.28	412	38.27	450	6.67	22.53	1927.56
Planform	0.30	7.91	375	37.98	413	7.27	23.56	1901.63
Compound	0.30	7.89	373	37.91	411	7.30	23.65	1903.41

Table 5.1: Comparison of Aircraft Aerodynamic Coefficients for the Winglet Designs at Cruise ($M = 0.85$ [-], $C_L = 0.3$ [-])

A comparison of the aerodynamic coefficients is provided in Table 5.1. Going from the winglet-off condition to the legacy winglet design, it is seen that the effect of adding the winglet decreases the aerodynamic efficiency of the aircraft by 2.9 %, producing the same lift at a larger angle of attack. The increase in drag is attributed

majorly to the difference in pressure drag while a very minimal decrease is observed in the friction drag even though an increase in the wetted area is observed. This anomaly however is also observed only when going from the planform optimized to the compound design. It could be hypothesized that for these designs, the local Reynolds number is increased leading to a change in the shape of the boundary layer which consequently decreases the skin friction coefficient. This decrease could offset the increase in wetted areas seen, leading to a smaller friction drag coefficient. From the baseline design to the compound design, the trends observed are similar with a steady drop in drag counts and angle of attack at which $C_L = 0.3$ is achieved. The aerodynamic efficiency of the baseline wing is increased by 2.32 %, and that of the planform optimized wing is increased by 11.54%, while the compound design increases this by 11.89 %, all with respect to the winglet-off case. As expected, the pressure drag is reduced by all the optimum winglet designs when compared with the winglet-off case. It must also be noted that the center of pressure x_p of the winglet designs is shifted aft of the aircraft nose when compared with the winglet-off case. It can be implied that the pitching moment characteristics of the more optimized designs are also improved steadily.

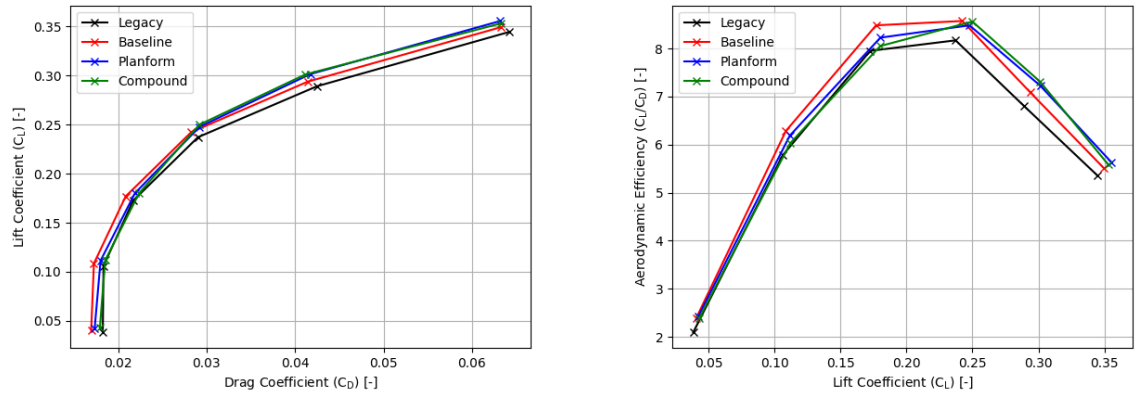

(a) Drag Polar at Cruise

(b) Aerodynamic Efficiencies for Varying Lift

Figure 5.1: Comparison of Aircraft Aerodynamic Polars for the Winglet Designs at Cruise ($M = 0.85$ [-], $C_L = 0.3$ [-])

The cruise drag polars for the different designs are compared in Figure 5.1a. The results of the optimization are again confirmed by these polars. All the modified designs outperform the legacy design at every lift coefficient, except for a small portion between $C_L = 0.15$ and $C_L = 0.2$, where it slightly outperforms the compound design, visible more clearly in Figure 5.1b. The baseline design performs better than the optimized winglets at lower lift coefficients, up till a value of $C_L = 0.25$. The compound design does not significantly outperform the planform design and in fact, only does better in the interval of $C_L = 0.25$ to $C_L = 0.3$. The optimized designs perform better than the other designs at higher lift coefficients and the difference when compared to the legacy design, is almost constant for the higher ranges. The maximum aerodynamic efficiency attained by these designs, however, is not at the lift coefficient but at a lower value. The baseline design has a maximum aerodynamic efficiency higher than the optimized designs and plateaus around the same lift coefficients as the optimized designs with the difference getting smaller at higher lift coefficients.

A comparison of the lateral-directional stability derivatives is provided in Table 5.2. It must be noted that all the force and moment coefficients obtained from SU2 [48] are used directly for the stability analysis. A body axis transformation is not made to the coefficients. The resulting stability derivatives are therefore applied in the wind axis. The yawing and rolling moment coefficients, C_{n_β} and C_{l_β}, due to sideslip, are obtained in this table from the sideslip polars as shown in Figure 5.2 for all the design cases. Similar to the optimization process, a first-order polynomial is fit using the least squares polynomial method to obtain the slopes of these

curves. Although it can be argued that this technique does not accurately represent the non-linearity observed in the stability derivatives, and is not ideally suited for an aerodynamic or flight control model, the magnitude of the linear fit slopes provide some sensitivity to the stability derivatives to be able to compare the performance of various winglet designs. Observing the yawing moment and rolling moment coefficient polars more closely, it is seen that the effect of sideslip on the rolling moment coefficient is relatively low and is almost linear in nature, even when considering the various design cases. This is also confirmed by the relatively small changes in C_{l_β} between the 4 designs.

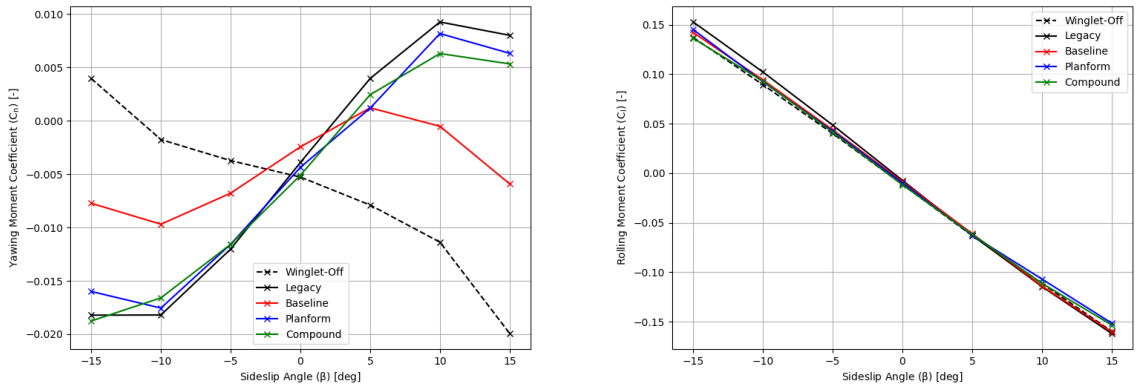

(a) Yawing Moment Coefficient

(b) Rolling Moment Coefficient

Figure 5.2: Comparison of Aircraft Sideslip Polars of Stability Coefficients for the Winglet Designs at Approach ($M = 0.22$ [-], $\alpha = 18$ [°])

The yawing moment coefficient on the other hand produces distinct features due to variation in sideslip. The implication on $C_{n_{\beta_{dyn}}}$ is that the sensitivity of this parameter is contributed to majorly by the C_{n_β}. This is backed up by the fact that the stability-optimized planform design benefits from an increased $C_{n_{\beta_{dyn}}}$ value due to the increase seen in C_{n_β}, while the value of C_{l_β} drops by 2.42 % compared to the baseline design. Comparing the slopes of the yawing moment coefficient curves, the unstable nature of the winglet-off case is predominant as confirmed by the negative C_{n_β} value and a positive C_{y_β}. The legacy design has the highest magnitude for all the stability derivatives indicating strong lateral-directional stability. The value of $C_{n_{\beta_{dyn}}}$ that it possesses is 50% larger than the target values that were defined for $C_{n_{\beta_{dyn}}}$ by Horwitz [14]. In fact, all the winglet designs including the winglet-off case depict a value significantly higher than this target.

Design	C_{y_β} $(\cdot e^{-4})$ [°$^{-1}$]	C_{n_β} $(\cdot e^{-4})$ [°$^{-1}$]	C_{l_β} $(\cdot e^{-4})$ [°$^{-1}$]	$C_{n_{\beta_{dyn}}}$ $(\cdot e^{-4})$ [°$^{-1}$]
Winglet-off	5.26	-6.79	-99.59	44.64
Legacy	15.85	10.69	-106.28	64.70
Baseline	10.46	2.27	-101.95	54.47
Planform	13.52	9.37	-99.48	59.57
Compound	13.87	9.44	-98.55	59.54

Table 5.2: Comparison of Aircraft Lateral-Directional Stability Derivatives for the Winglet Designs at Approach ($M = 0.22$ [-], $\alpha = 18$ [°])

Although for the winglet-off case, this target value is met, it only implies that the aircraft may be dynamically stable in lateral-directional motion, since the value of C_{n_β} is still negative, implying static instability in yaw as mentioned before. It seems that the contribution to $C_{n_{\beta_{dyn}}}$ for the winglet-off case is influenced by

the terms for C_{l_β} in the equation for $C_{n_{\beta_{dyn}}}$, providing it with a higher weight, leading to the target value being met. The winglet-off case also exhibits a strong static lateral stability, further adding the cause for this effect. It also confirms Benad's [6] initial findings about the inherent nature of the Flying-V being laterally stable but not directionally stable. This also provides an example as to to the definition of the objective made previously that the value of $C_{n_{\beta_{dyn}}}$ is used only to amplify the lateral-directional stability, but does not necessarily guarantee stability in the disparate motions.

A significant drop of 15.81 % in the value of $C_{n_{\beta_{dyn}}}$ is observed when going from the legacy to baseline design, considering the aerodynamic efficiency improvement was limited to 5.37 %. For the baseline design, this drop also signifies the relatively small region of sideslip angles within which it is stable. From Figure 5.2a it can be seen that the linear effects are only produced between β = -10 and β = 5 and that the non-linear effects are more significant in a positive sideslip. The planform-optimized design is able to recover the stability objective from the baseline design by 9.36% but still lags behind the legacy design's value by 7.92 %. It is interesting to note that even though the stability objective was not considered in the airfoil optimization step, the compound design poses slightly higher stability coefficients except for $C_{n_{\beta_{dyn}}}$ with only a 0.05 % difference. This also confirms the assumption made while defining the optimization process that the airfoil shape's effect on the stability performance is either negligible or not negatively impacted by an aerodynamic optimization routine.

Design	r_b [m]	b [m]	λ [-]	Λ [°]	ϕ [°]	ϵ_r [°]	ϵ_t [°]	$(t/c)_r$ [%]	$(t/c)_t$ [%]
Legacy	0.50	7.00	0.50	30.00	10.00	0.00	0.00	9.69	9.69
Baseline	1.00	5.00	0.40	40.00	20.00	-3.00	2.00	9.69	9.69
Planform	1.99	5.48	0.61	32.40	24.08	9.22	-4.96	9.69	9.69
Compound	1.99	5.48	0.61	32.40	24.08	4.23	9.14	10.38	11.00

Table 5.3: Comparison of Design Variables of the Winglet Designs

Changes in the force and moment coefficients can be correlated to the changes made to the winglet design variables during the optimization process. The winglet design variables for the various designs are listed in Table 2. When comparing the cost function results for the planform optimization process, with an increase of 9.36 % in the stability objective compared to an 8.99 % increase in the aerodynamic objective, implications of the minor bias towards the stability objective can be seen. This is also visible in the design parameters of the planform design. The optimizer tends to increase both the blend radius and the winglet span to try to maximize the vertical distance, which is favourable from a stability perspective. However, it does not go all the way towards the upper bound of the winglet span but is closer to the upper bound of the blend radius. The optimizer is able to find a solution that has a higher value in both objectives without excessively increasing the span. This is in contrast to Horwitz's [14] findings that displayed a sample space that was heavily influenced by the winglet span. The increase in taper ratio and reduction in sweep angle could also be associated with this fact, that the stability objective drives its values but seems to be balanced by an increased cant angle.

5.2 Flow Physics Assessment at Cruise Conditions

A comparison of the airflow characteristics for each of the winglet designs is presented at cruise conditions. The pressure distributions presented are evaluated on the same grid as used for the optimization. It can be argued that this deviates from or does not provide the actual flow physics over each of the winglet designs, especially since the initial grid used was tuned to a particular geometry. Whereas more specific flow features

could be obtained from a finer grid more accurately, the aim is to also build a cause-and-effect relationship with the flow physics and winglet geometry, keeping the optimizer in mind, essentially seeing the solutions as the optimizer "sees" it. While the optimizer does not comprehend the detailed flow characteristics of the designs, it does pick up on sensitivities in the objective functions. Ultimately, the goal is to understand what flow features represented on this grid level cause the sensitivities seen in the objective function by the optimizer. Pressure distributions and contours for the legacy design are first compared with the baseline design, and in succession, the optimized designs are compared to the baseline design. The pressure contours over the outer wing and winglet are presented in Figure 5.3 and Figure 5.6.

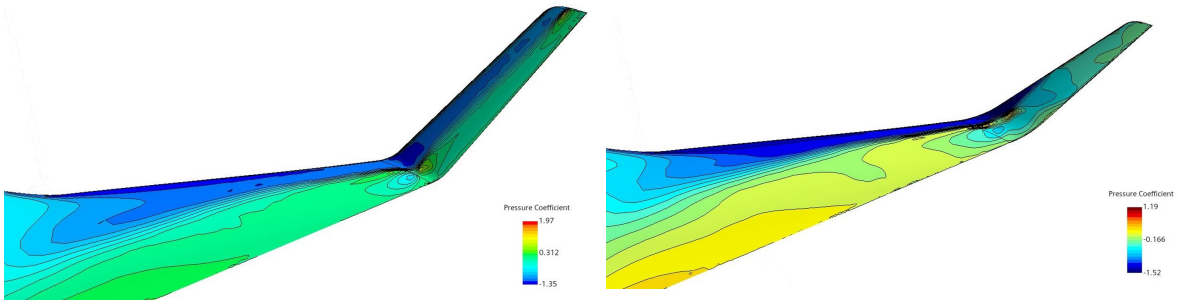

(a) Legacy Design

(b) Baseline Design

Figure 5.3: Comparison of Pressure Coefficient Contours over the Outer Wing with the Initial Winglet Designs at Cruise ($M = 0.85$ [-], $C_L = 0.3$ [-])

The legacy design seems to have a constant shock wave sitting on the leading edge of the winglet, continuing all the way from the outer wing as seen in Figure 5.3a. The magnitude of the shock gets worse at the blend trunk, where the isobars are severely pinched. This region produces a strong shock-induced separation, which is also confirmed in Figure 5.4a at 50 % x/c in the region of the blend trunk, where the pressure increases rapidly. This effect is reduced by going slightly higher up the winglet where the shock ends a bit more gradually as seen in Figure 5.4b.

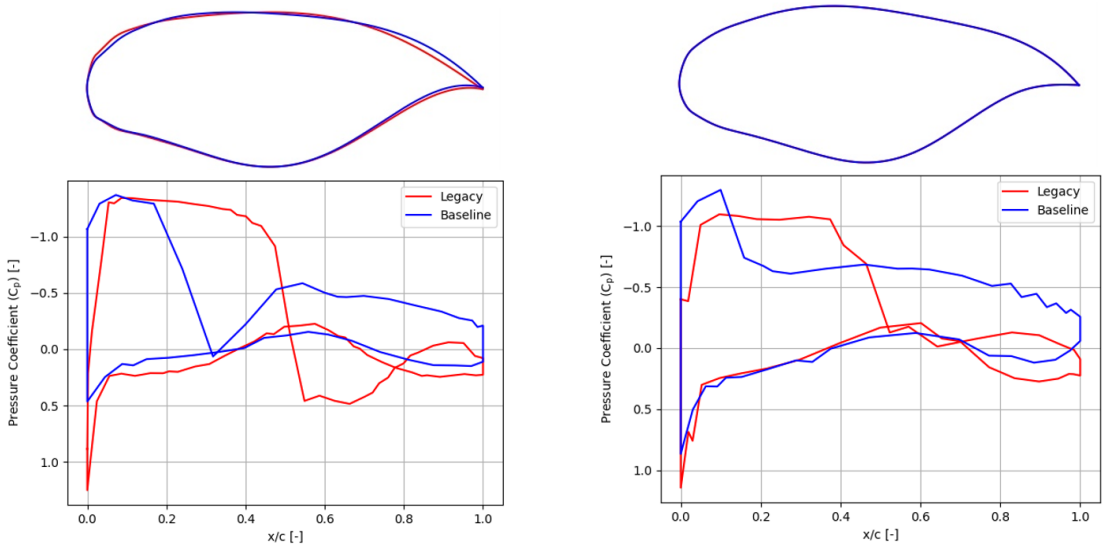

(a) $\eta_{7.5}$

(b) η_{35}

Figure 5.4: Comparison of Pressure Coefficient Distributions over the Legacy and Baseline Designs Closer to the Winglet Root ($M = 0.85$ [-], $C_L = 0.3$ [-])

A similar effect is seen in the baseline design in Figure 5.3b, except that the shock, even though has a similar magnitude, terminates much earlier as also confirmed by Figure 5.4a. The flow re-attaches itself for both designs at different extents, and the baseline design seems to produce more lift on the aft portion at this spanwise location $\eta_{7.5}$ compared to the legacy design. At η_{35}, the baseline design has the shock terminating much earlier and more gradually compared to the legacy design, and also has a higher suction peak as can be seen in Figure 5.4b. On the legacy design, the shock continues all the way to the tip and terminates again with a shock-induced separation region as seen in the pressure contours Figure 5.3a and the pressure distribution at the tip in Figure 5.5b. For a majority of the mid-section of the legacy winglet, the shock is evenly distributed looking at the pressures in the spanwise direction. The uniform pressure contours in this section produce similar pressure distributions at η_{35} and η_{65}. The baseline design has the shock terminating at close to 50 % of the span. At a spanwise location before the termination of the shock and after the wing tip, there is another point of shock-induced separation, this time more significant also in the spanwise direction. This effect causes a completely separated wake over the rest of the baseline winglet's tip and is also seen in the pressure distributions in Figure 5.5a and Figure 5.5b. The airfoil shapes for both the legacy and baseline design do not differ significantly from each other, considering no changes were made in the CST coefficients going from the legacy to the baseline design.

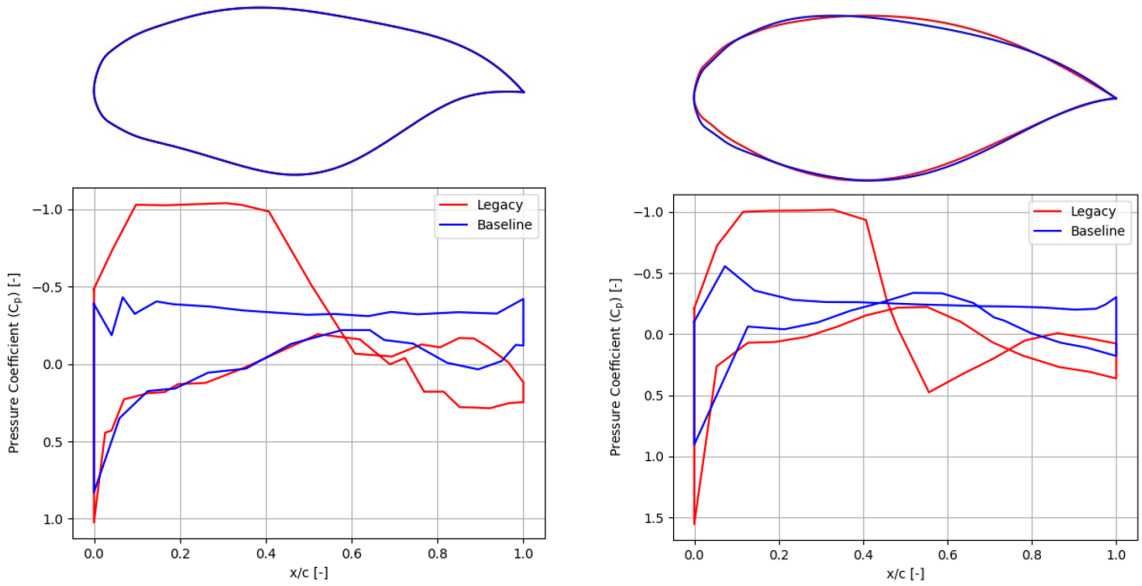

(a) η_{65}

(b) η_{95}

Figure 5.5: Comparison of Pressure Coefficient Distributions over the Legacy and Baseline Designs Closer to the Winglet Tip ($M = 0.85$ [-], $C_L = 0.3$ [-])

The decrease in winglet sweep for the planform design leads to the shock wave that was almost non-existent on the baseline design as seen in Figure 5.3b to sit almost at a constant spanwise location close to the leading edge as seen in Figure 5.6a similar to the legacy design and can also be seen in Figure 5.7a and Figure 5.7b. Although the shock is now extended along the chordwise direction, the optimizer seeks to reduce the shock-induced separation that was seen at the end of the blend section on the baseline design. The effect of increasing the blend radius and the cant angle seems to have a positive effect on this in the planform design as the adverse pressure gradient that was seen on the baseline design is now significantly reduced with a more gradual pressure rise behind the shock as also seen in Figure 5.7a and Figure 5.7b. The planform design maintains the suction peak throughout the winglet span as seen in all spanwise stations. The shock size seems to continue from the outer wing onto the blend section and reduce to a constant gap moving spanwise towards

the winglet tip.

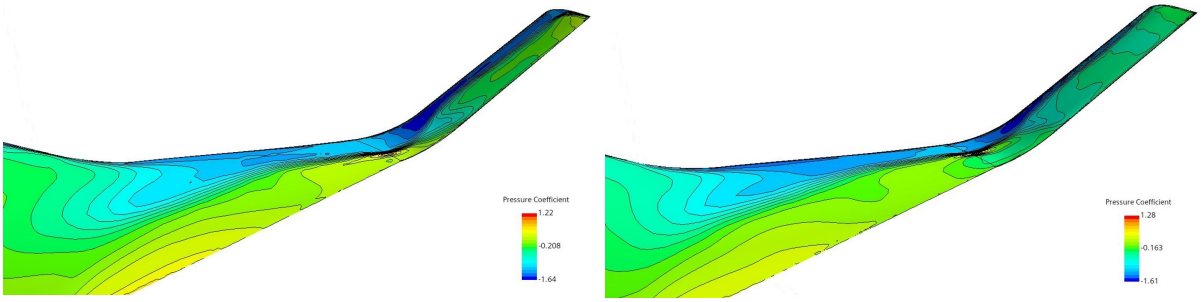

(a) Planform Optimized Design

(b) Compound Optimized Design

Figure 5.6: Comparison of Pressure Coefficient Contours over the Outer Wing with the Optimized Winglet Designs at Cruise ($M = 0.85$ [-], $C_L = 0.3$ [-])

This causes a majority of the lift on the planform design to act closer to the root. Although most of the lift is produced in the front for this design, the transitioning of the shock wave at η_{35} seems to produce significantly more lift on the aft compared to other spanwise locations. This may be also attributed to the fact that a quick reattachment is seen in this section at 75 % chordwise direction shown in Figure 5.7b.

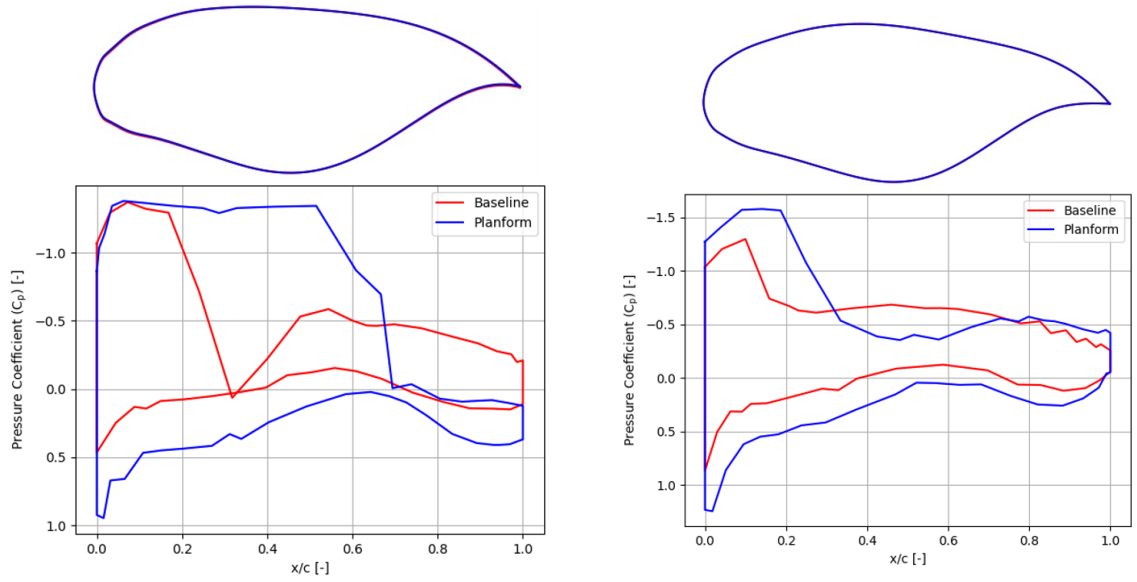

(a) $\eta_{7.5}$

(b) η_{35}

Figure 5.7: Comparison of Pressure Coefficient Distributions over the Baseline and Planform Designs Closer to the Winglet Root ($M = 0.85$ [-], $C_L = 0.3$ [-])

An almost similar effect is seen at η_{65} shown in Figure 5.8a for the planform design, but here, aft of the shock the rear loading is much lower compared to spanwise station η_{35}. The pressure distribution on the pressure side for both the baseline and planform optimized design is similar at η_{95}. On the suction side, however, the planform design again sees a stronger gradient behind the shock, with the shock getting stronger in magnitude. This is attributed to the tip effect, but unlike the legacy design, the Kuchemann tip design for the planform winglet bends the isobars towards the tip causing a relatively smoother pressure rises behind the shock as seen in Figure 5.8b and Figure 5.5b. Again, as in the case of the legacy and baseline comparison, the planform design also shows no difference in the spanwise location's airfoil shapes. The planform design shows a wash-in twist distribution on the blend section until the winglet root and from the root to the tip, a wash-out distribution. It is unclear as to the cause for this, but it is hypothesized that the optimizer is trying

to balance the increase in taper ratio that is clearly necessitated by the stability objective by rapidly varying the twist values. And as the winglet twist was seen to have limited sensitivity on the objectives, the wash-out that is seen might merely be a locally bound optimum value in the context of the other planform parameters.

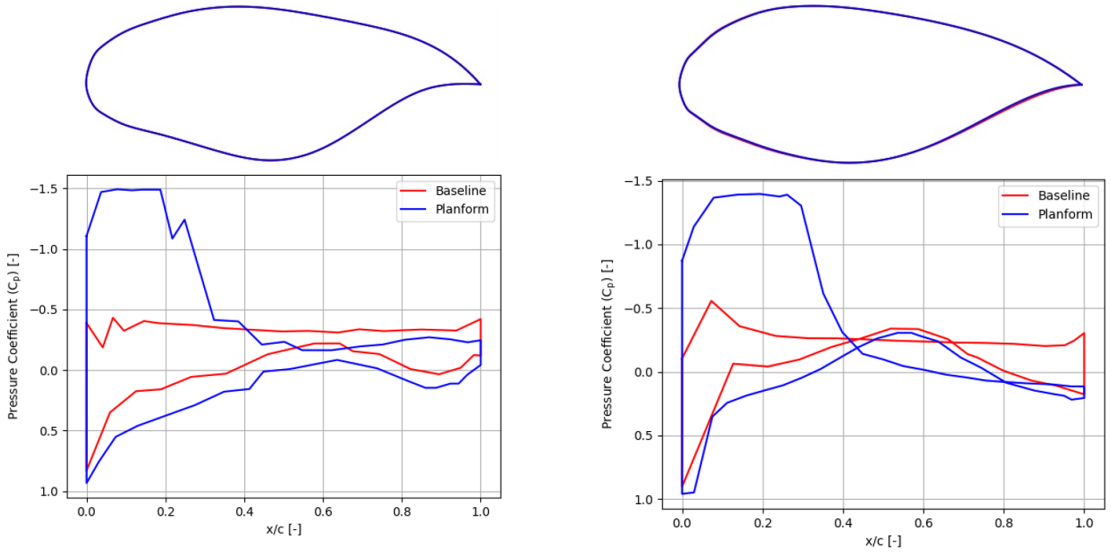

(a) η_{65} (b) η_{95}

Figure 5.8: Comparison of Pressure Coefficient Distributions over the Baseline and Planform Designs Closer to the Winglet Tip ($M = 0.85$ [-], $C_L = 0.3$ [-])

The compound-optimized design seeks to reduce the strength of the shock wave seen on the planform optimized winglet as seen in Figure 5.6b. While the shock-induced separation on the baseline design disappears on the compound winglet closer to the winglet root at η_{35}, the compound design also further reduces the pressure gradient behind the shock compared to the planform design as seen in Figure 5.9b.

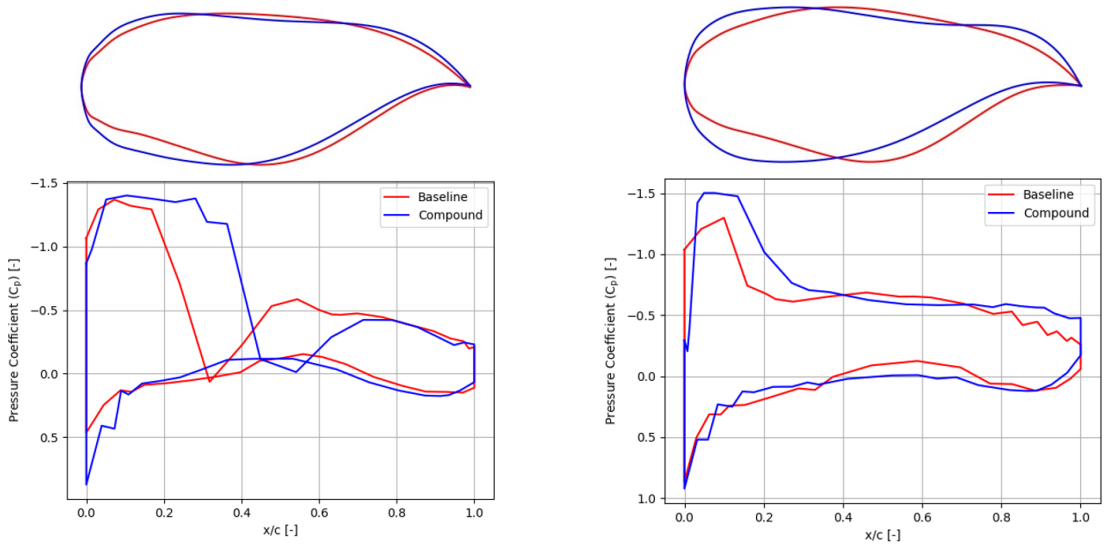

(a) $\eta_{7.5}$ (b) η_{35}

Figure 5.9: Comparison of Pressure Coefficient Distributions over the Baseline and Compound Designs Closer to the Winglet Root ($M = 0.85$ [-], $C_L = 0.3$ [-])

The pinched lambda-shock at the wing tip root however still can be seen. An implication of imposing minimum structural thickness constraints during the airfoil optimization is that the optimizer increases the leading edge radii of the airfoils closer to the outer wing tip, on the blend and winglet root, as seen in Figure 5.9a and Figure 5.9b. At the blend section $\eta_{7.5}$, the optimizer tends to introduce some concavity to the suction side of the airfoil. This could be in an attempt to increase the pressure behind the shock, creating a less adverse pressure gradient. A similar approach is taken at the winglet root, where the concavity is more pronounced, however, the trailing edge slope is more steep compared to the blend section. While this seems like a viable solution going closer to the winglet root, which has a smoother pressure rise aft of the shock seen in Figure 5.9b, closer to the outer wing tip, the pressure rise is steeper and potentially causes a separation bubble, as the flow reattaches a further aft in the chordwise direction as seen in Figure 5.9a. At the compound design's winglet tip and kuchemann tip, the trailing edge slope is very steep as shown in Figure 5.10a and Figure 5.10b. This leads to the separated flow at the winglet's tip as seen in Figure 5.10a and Figure 5.10b. Due to a thicker tip section on the airfoil-optimized winglet, the amount of lift extracted at the tips is also higher compared to any of the winglet designs.

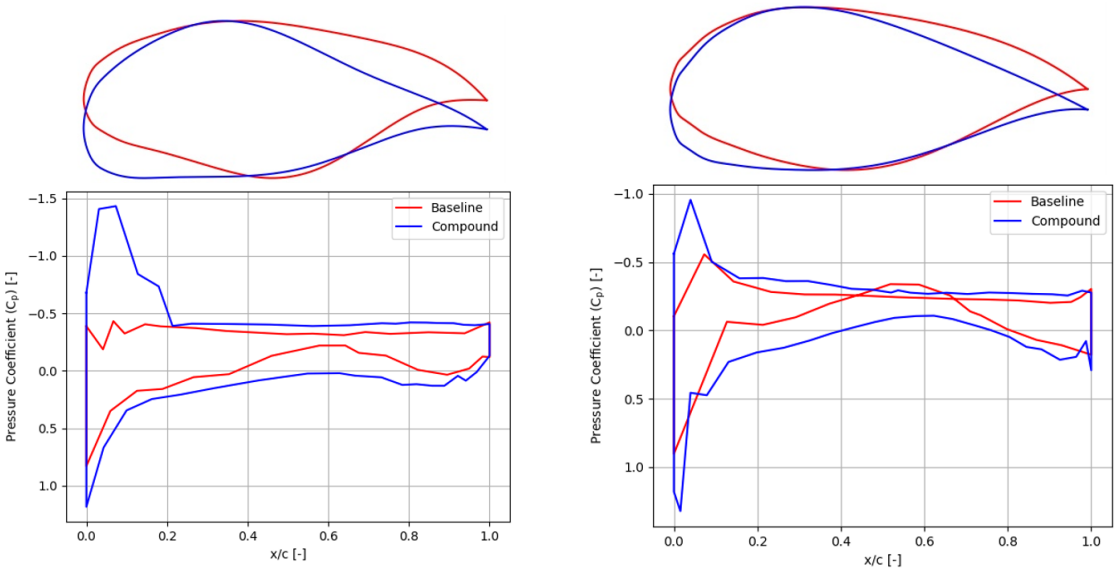

(a) η_{65}

(b) η_{95}

Figure 5.10: Comparison of Pressure Coefficient Distributions over the Baseline and Compound Designs Closer to the Winglet Tip ($M = 0.85$ [-], $C_L = 0.3$ [-])

5.3 Flow Physics Assessment at Approach Conditions

Similar to the cruise condition, the flow over the different designs is compared this time in the approach conditions. The same methods and grid sizes are used as explained previously in the following analysis.

5.3.1 Investigation of Non-linear Behaviour in Aircraft Yaw

It was found in section 5.1 that the FV-1000 had an inherent non-linear behaviour in its yawing moment coefficient due to varying sideslip angles, regardless of the winglet design used if any. Particularly at high sideslip angles, almost all designs tended to become less stable, exhibiting stall-like behaviour typically seen in lift polars. An investigation was done in order to correlate this occurrence to flow characteristics over the

aircraft. The baseline case exhibits the most non-linear behaviour compared to all the designs, irrespective of their magnitudes. For this reason, the baseline design was used as the platform to conduct this investigation. Sideslip angles of $\beta = 5$ [°] and $\beta = 15$ [°] were chosen as the operating conditions for this analysis as they portray the extremities of the yawing moment coefficient value for a positive sideslip angle range.

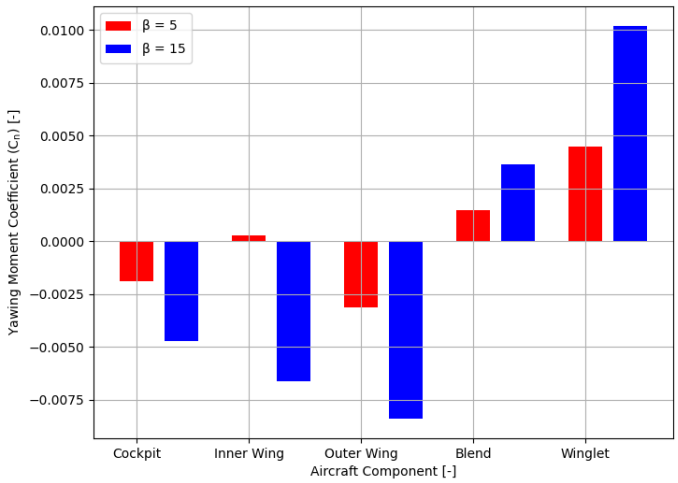

Figure 5.11: Aircraft Component Breakdown of Yawing Moment Coefficients for Nominal and Limiting Sideslip Cases ($M = 0.22$ [-], $\alpha = 18$ [°])

Along the aircraft, the different components can display varying behaviours in yawing moment variation with sideslip. To identify the source of the inflection points seen in Figure 5.2 and the component contributing to this, a breakdown of yawing moment coefficients for the various aircraft components is plotted at the two sideslip angles in Figure 5.11. At both sideslip angles, the cockpit and the outer wing produce destabilizing characteristics, and their magnitude only increases when going from $\beta = 5$ [°] to $\beta = 15$ [°]. The blend section and the winglet section (separated here to make a distinction in yaw behaviour) produce the opposite effects, stabilizing the aircraft, and also increasing the magnitude of the yawing moment at higher sideslip angles. The inner wing produces a negligibly small stabilizing yawing moment at $\beta = 5$ [°] and $\beta = 15$ [°] but switches its behaviour drastically at $\beta = 15$ [°] causing very strong destabilizing moments. Its contribution at $\beta = 15$ [°] causes the imbalance in opposing yawing moments between the rest of the components, which otherwise would cause the aircraft to be neutrally stable when comparing their magnitudes at the two operating conditions.

To dive a step deeper into the source of the particular contributions from each of the components, the flow characteristics at the two operating points are also investigated. In Figure 5.12, the skin friction coefficient contours are compared over the suction side of the entire aircraft at $\beta = 5$ [°] and $\beta = 15$. It can be seen that at $\beta = 5$ [°] there is a region of separation of the flow on the port side of the cockpit and centre fairing. This region grows drastically at $\beta = 15$, causing the flow to be separated almost fully. This causes the cockpit to produce a force that puts the aircraft in the direction of the sideslip, i.e. a destabilizing moment. For the inner wing, at $\beta = 5$ [°], the flow over a large portion of the port wing is still attached with some separation also on the starboard side. This may be causing sufficient balance in the forces between the wings, causing a net stabilizing effect on the aircraft. On the contrary, the outer wing has a fully separated port wing in both cases and to add to this sees a more attached flow at $\beta = 15$ [°] on the starboard wing due to the inflow angle being oriented more towards the direction of the wing, reducing the effect of the wing sweep and causing higher loads on it.

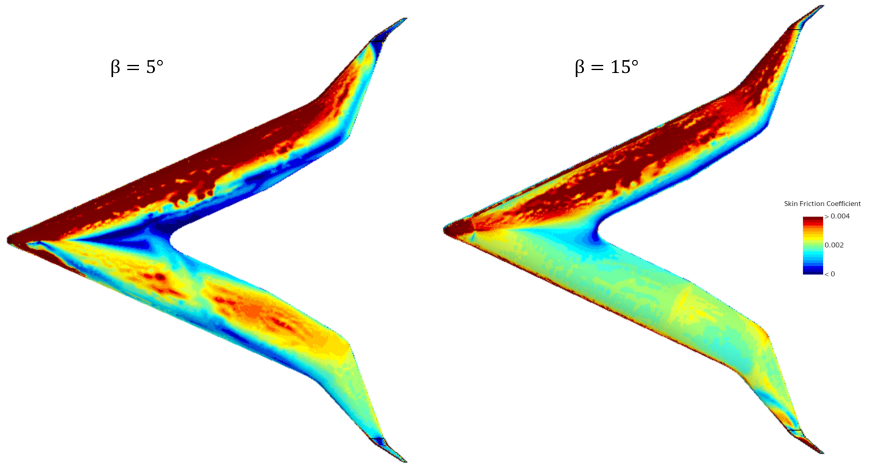

Figure 5.12: Skin Friction Coefficient Contours over the Aircraft at Nominal and Limiting Sideslip Cases (M = 0.22 [-], α = 18 [°])

A similar comparison is made for the winglets at the two operating points in Figure 5.13a, Figure 5.13b, for the port side winglet, and Figure 5.14a, Figure 5.13b, for the starboard winglet, this time also including pressure distributions. This comparison is particularly important for the Flying-V's winglets as the airfoils are asymmetric and can contribute to opposing side forces in asymmetric conditions. The goal of the winglet design to act also as the vertical stabilizer, in this case, must be to limit the side force on the symmetric component depending on the direction of the destabilizing flow so that the net effect from the winglets is positive on the winglets.

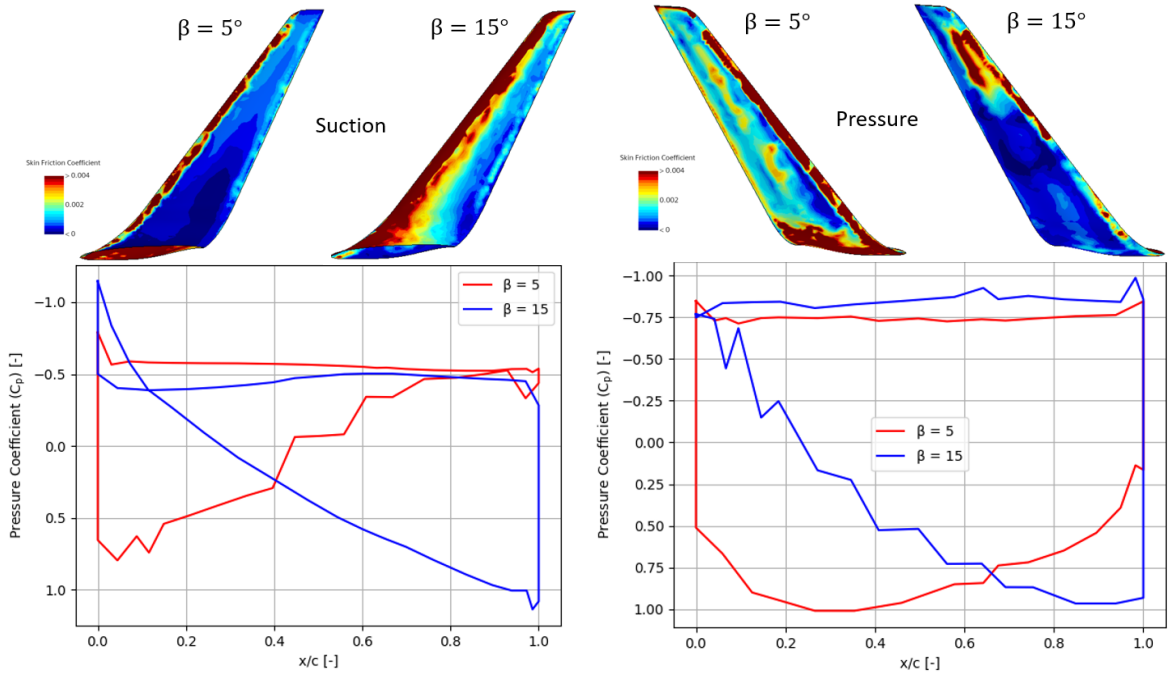

(a) $\eta_{7.5}$ (b) η_{65}

Figure 5.13: Comparison of Pressure Distributions and Skin Friction Coefficient Contours on the Starboard Winglet at Nominal and Limiting Sideslip Cases (M = 0.22 [-], α = 18 [°])

The net positive yawing effect from the winglets can be ascertained from the skin friction polars on the winglet. On the starboard side, the flow is more attached at β = 15 [°] compared to β = 5 [°], which also

causes higher suctions peaks on the winglet as can be seen in Figure 5.13a. The amount of loading on the starboard winglet is also higher at a further spanwise location as seen when comparing Figure 5.13a and Figure 5.13b.

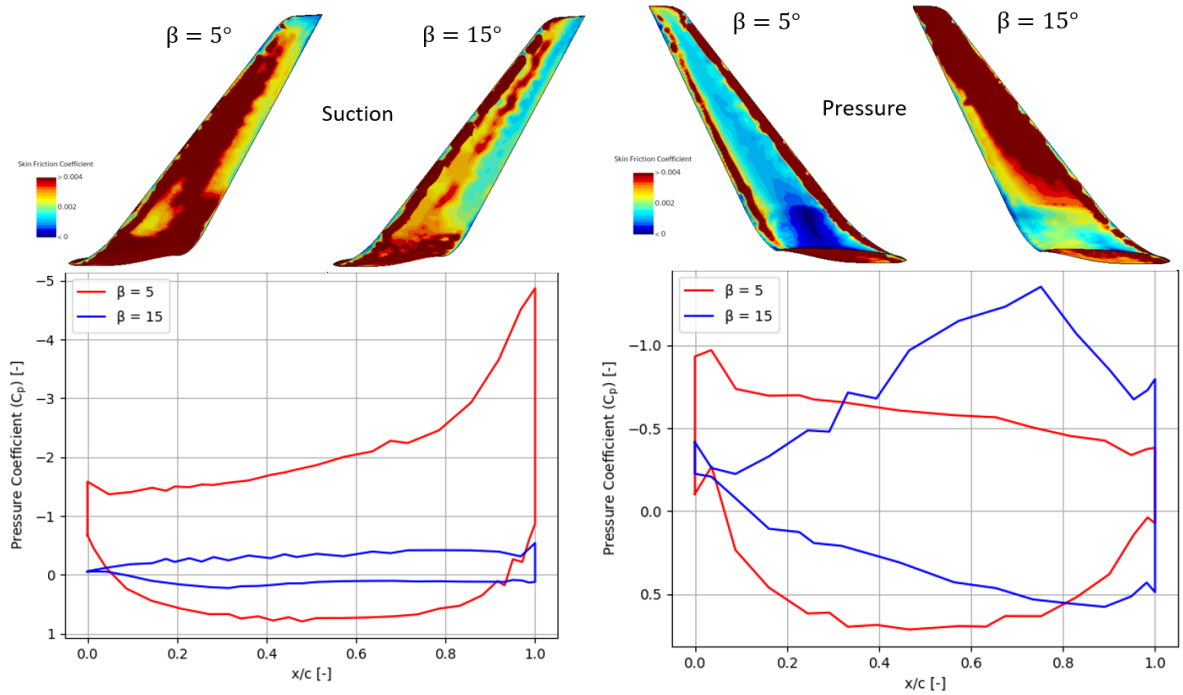

(a) $\eta_{7.5}$ (b) η_{65}

Figure 5.14: Comparison of Pressure Distributions and Skin Friction Coefficient Contours on the Port Winglet at Nominal and Limiting Sideslip Cases ($M = 0.22$ [-], $\alpha = 18$ [°])

On the port winglet, the airflow shifts from being more attached on the suction side to being more attached on the pressure side when going from $\beta = 5$ [°] to $\beta = 15$ [°]. This leads to a lower loading on the port winglet at $\beta = 15$ [°] as seen in the pressure distributions in Figure 5.14a and Figure 5.14b compared to the winglet at $\beta = 5$ [°]. This is a positive effect in terms of the stabilizing side force as the port wing contributes lesser leading to a lower opposing side force.

5.3.2 Comparison of Flow Features over Winglet Designs

The techniques used in the previous section are repeated to analyse the performance of the winglet designs in the approach phase design point. Comparing the legacy design with the baseline design, it can be seen in Figure 5.15 that the legacy design and the baseline design almost have a similar flow pattern on the starboard winglet when looking at the skin friction contours. The loading on each of the winglets is also very similar when looking at the areas covered by the pressure distributions, with the legacy design producing slightly higher suction peaks. On the port wing, the situation is different, with the flow patterns over the baseline designs being more attached than the legacy design as shown in Figure 5.16. The loading on the baseline design is significantly larger compared to the legacy design when looking at the pressure plots even though the legacy design produces a larger suction peak at η_{65} in Figure 5.16b. A large portion of the pressure side on the blend section on the legacy design has a separated region causing the loads to act mainly from the winglet tip, which is also confirmed by the pressure distribution at η_{65} in this region. It can be inferred that the source of the lower yawing stability on the baseline design is predominantly due to the opposing side force generated by the port side winglet.

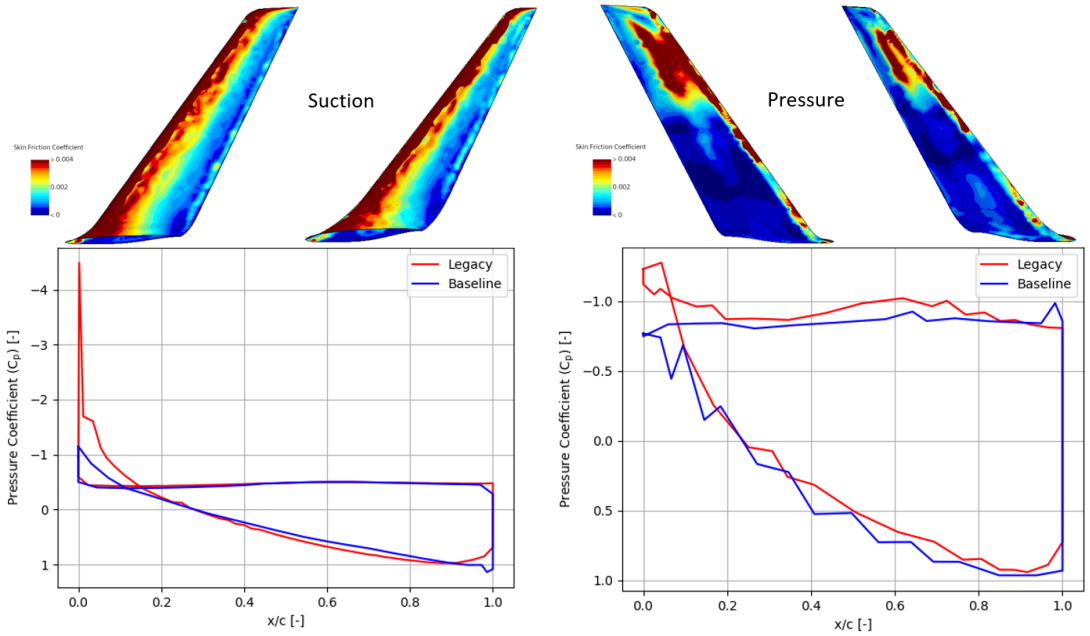

(a) $\eta_{7.5}$ (b) η_{65}

Figure 5.15: Comparison of Pressure Distributions and Skin Friction Coefficient Contours on the Starboard Winglet for the Legacy and Baseline Designs ($M = 0.22$ [-], $\alpha = 18$ [°], $\beta = 15$ [°])

A similar scenario is seen when a comparison is made with the planform and compound designs, with respect to the baseline design on the starboard winglet in Figure 5.17 and Figure 5.19, and the port winglets in Figure 5.18, and Figure 5.20. The planform and the compound designs both produce higher suction peaks compared to the baseline on the starboard wing. It is interesting to note that the difference in the flow patterns over the planform and the compound winglets are not significantly different.

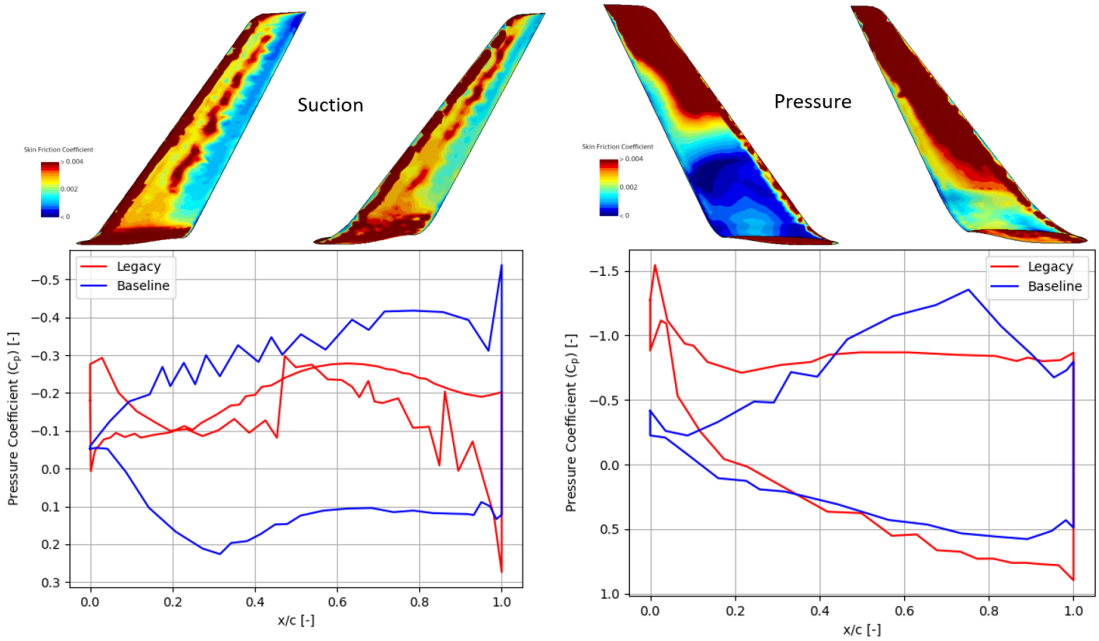

(a) $\eta_{7.5}$ (b) η_{65}

Figure 5.16: Comparison of Pressure Distributions and Skin Friction Coefficient Contours on the Port Winglet for the Legacy and Baseline Designs ($M = 0.22$ [-], $\alpha = 18$ [°], $\beta = 15$ [°])

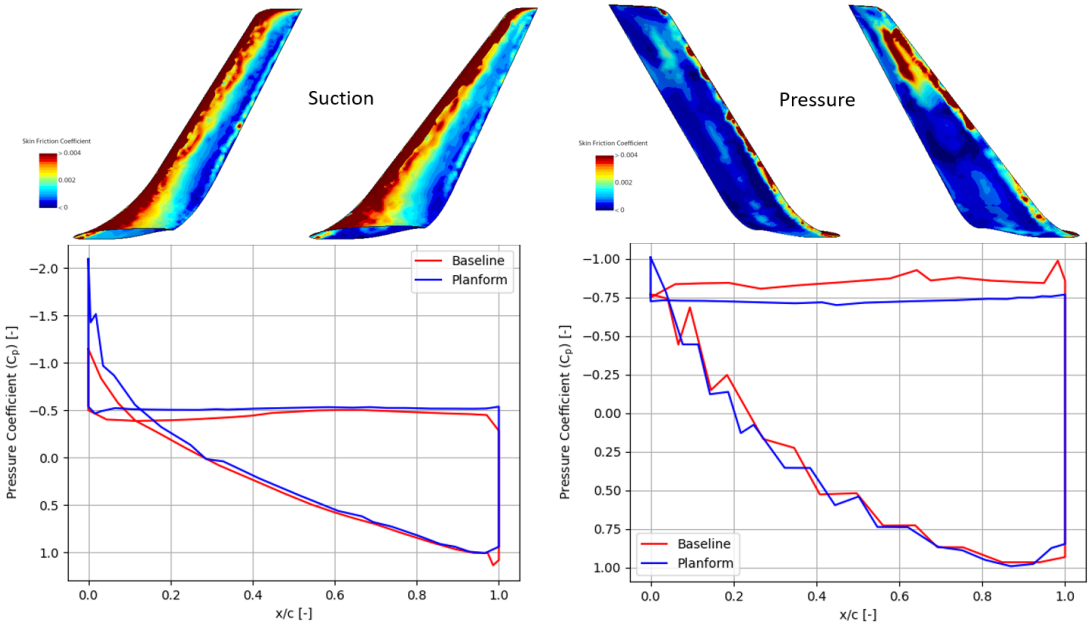

(a) $\eta_{7.5}$ (b) η_{65}

Figure 5.17: Comparison of Pressure Distributions and Skin Friction Coefficient Contours on the Starboard Winglet for the Baseline and Planform Designs ($M = 0.22$ [-], $\alpha = 18$ [°], $\beta = 15$ [°])

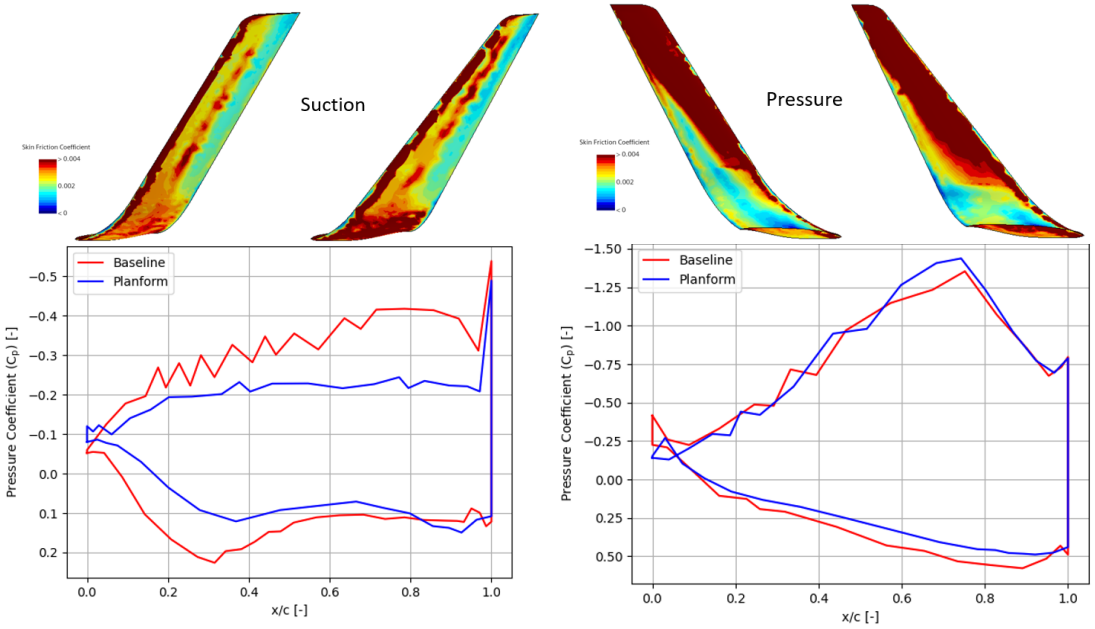

(a) $\eta_{7.5}$ (b) η_{65}

Figure 5.18: Comparison of Pressure Distributions and Skin Friction Coefficient Contours on the Port Winglet for the Baseline and Planform Designs ($M = 0.22$ [-], $\alpha = 18$ [°], $\beta = 15$ [°])

If we compare Figure 5.18b and Figure 5.20 we see that the region of separation on the pressure side of the planform winglet is slightly larger than on the compound winglet leading to the difference in yawing moment coefficient seen in Figure 4.8b. It must be noted that a pattern ultimately emerges in the source of differences in the yaw stability. Although it is attributed to the differences in the flow pattern on the port side winglets, narrowing it down further to the spanwise locations on the port winglet we see that on all the winglet designs the blend regions show the most differences in the amount of loading with respect to each other.

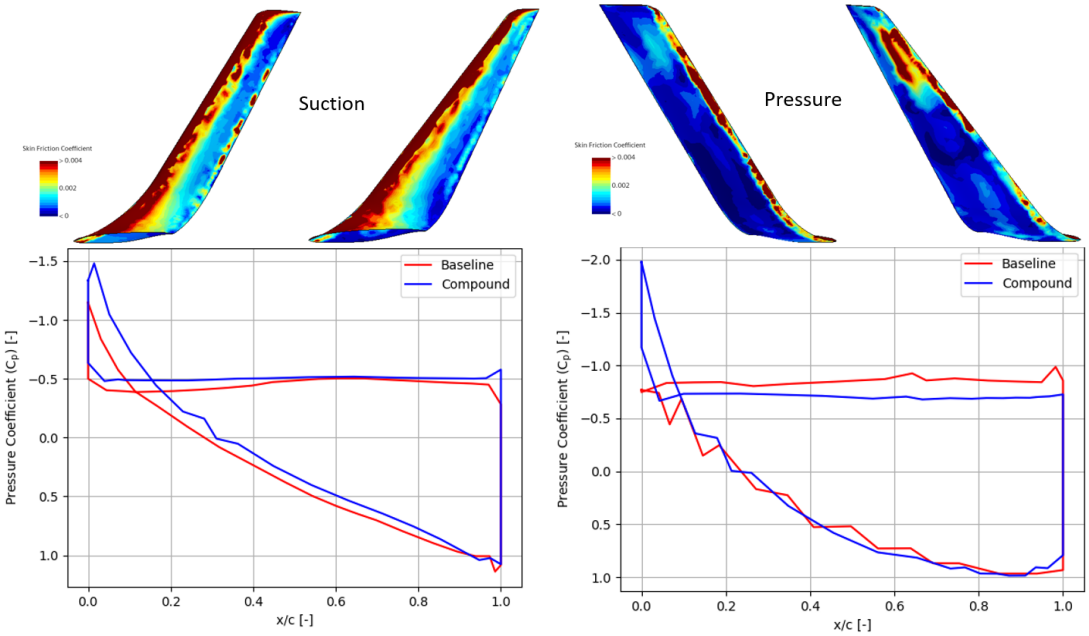

(a) $\eta_{7.5}$ (b) η_{65}

Figure 5.19: Comparison of Pressure Distributions and Skin Friction Coefficient Contours on the Starboard Winglet for the Baseline and Compound Designs ($M = 0.22$ [-], $\alpha = 18$ [°], $\beta = 15$ [°])

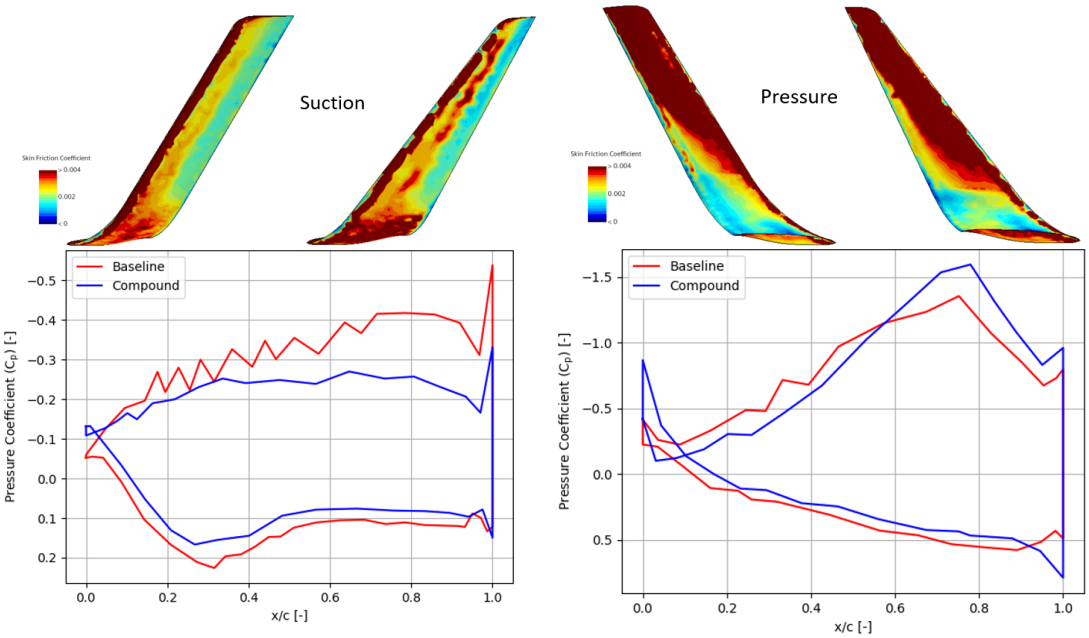

(a) $\eta_{7.5}$ (b) η_{65}

Figure 5.20: Comparison of Pressure Distributions and Skin Friction Coefficient Contours on the Port Winglet for the Baseline and Compound Designs ($M = 0.22$ [-], $\alpha = 18$ [°], $\beta = 15$ [°])

5.4 Preliminary Rudder Performance Assessment

A preliminary polar assessment was conducted with the baseline rudder design that was parameterized in subsection 3.1.3. The aircraft with rudders deflected at $\pm$ 30 [°] on the fully optimized compound winglet design were analysed. The same range of sideslip angles used for the stability analysis was used to simulate

varying steady heading sideslip conditions. The results of the side force due to sideslip polars and the yawing moment coefficient due to sideslip polars are plotted for the two rudder deflections in Figure 5.21a and Figure 5.21b respectively.

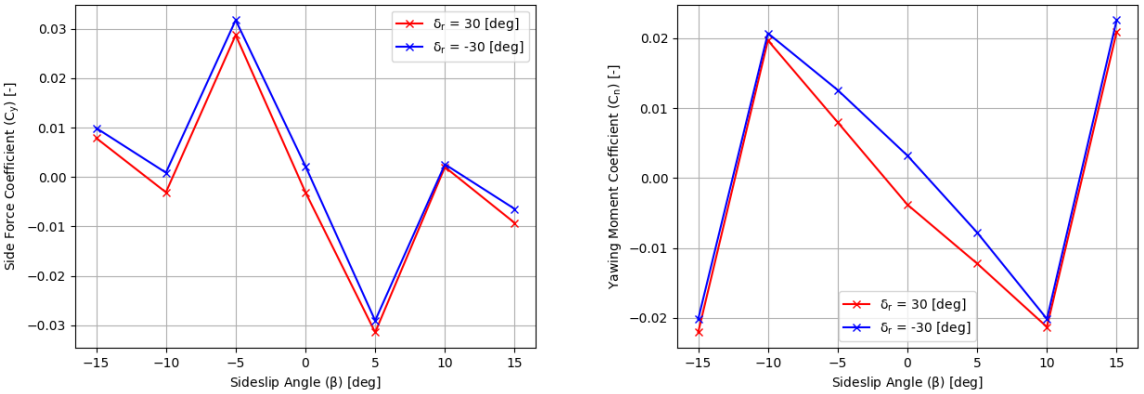

(a) Side Force Coefficient

(b) Yawing Moment Coefficient

Figure 5.21: Comparison of Aircraft Sideslip Polars of Yaw Stability Coefficients for Maximum Rudder Deflections During Approach ($M = 0.22$ [-], $\alpha = 18$ [°])

At first glance, it can be seen in Figure 5.21b that the yawing moment coefficient behaviours are symmetric for the two rudder deflections. The non-linearities found in the stability cases are observed again in the rudder-deflected cases on the aircraft. This is to be expected as the non-linear behaviour is an inherent nature of the aircraft itself. The differences in the symmetric rudder deflection cases reduce at the extreme sideslip conditions. The differences in the yawing moment coefficient are the greatest at zero sideslips and gradually reduce and are almost identical at the limiting sideslip case. This behaviour is also seen in the side force coefficient polar in Figure 5.21a. The differences between the two rudder deflections however are not consistent in the side force polars seen. It can be observed from these polars that the rudders are ineffective in stabilizing the aircraft from the sideslip making the aircraft more unstable going from zero sideslip to a sideslip angle of $\beta = 10$ [°]. The non-linear behaviour now seems to be a positive effect on the aircraft as the rudders make the aircraft jump from a fully unstable condition to a stable one going to the extreme sideslip case. Although a detailed flow pattern analysis is not made during this research, we can attempt to extrapolate the observations made in the previous sections for the stability analysis to the present case. It can be hypothesized that during positive sideslip cases, the starboard side winglet with the rudder is initially unable to balance the opposing moments from the port winglet and rudder, caused possibly by the asymmetric airfoil shape. But as the sideslip angle changes, the inflow angle on the aircraft causes the port side winglet to completely separate due to the flow direction and airfoil shape. On the starboard side, the winglet could get more effective due to the higher sideslip angle, and without a balancing moment from the port winglet, it ultimately causes the aircraft to become highly stable.

Chapter 6

Conclusions

The present study aimed to measure the cruise aerodynamic performance and lateral-directional stability characteristics in field flight for the Flying-V with winglets using RANS computations. The existing winglet trickling down from previous studies displayed poor aerodynamic performance but strong lateral-directional stability. The static directional instability of the Flying-V without winglets as found by preliminary studies was confirmed by the higher fidelity analyses. A sensitivity analysis of the winglet's design parameter showed the strong codependency of the parameter's effect on each other, with the winglet twist being unperturbed by their effect and having a relatively small impact on the objective functions. The sample design space generated from this analysis also brought forth a baseline design with improved cruise aerodynamic efficiency and a smaller span. The library developed catering to the winglet optimization as an extension to the existing Flying-V MMG was successfully used to perform single and multi-objective optimizations of the baseline winglet. Long run times of the RANS-based analysis limited the scope of the stability polars used for the stability optimization. A trickle-down effect of this led to a smaller population size being assessed during the multi-objective optimization of the winglets. The planform-optimized design improved the dynamic yawing moment coefficient due to sideslip compared to the initial design by 9.36 %, and by 11.54 % in aerodynamic efficiency relative to the winglet-off scenario. The planform winglet design tended to distribute the lift throughout the span by placing the shock at a constant chordwise section throughout the span. In addition, it attempted to obtain smoother pressure gradients behind the shock. Contradictory to previous studies, it was found that an increase in lateral-directional stability can be obtained without an excessive increase in winglet span. The airfoil optimization results in a design that is improved by 11.89 % relative to the winglet-off case, but is not significantly better than the planform design when also considering off-design conditions. The airfoil-optimized winglet attempted to maintain the nature of the platform-optimized winglet but attempted to reduce the strength of the shock on the leading edge. It was seen that all the winglet designs suffered from a shock-induced separation at the outer wing tip and the blend section. The planform optimization process tended to solve this issue by increasing the cant and blend radius. While the shock-induced separation was eliminated on the blend section, the pinched isobars seen on the wing tip in all designs were still maintained, indicating the need to include the outer wing tip airfoil parameters in the airfoil optimization step of the winglets. Structural thickness constraints imposed on the airfoil were found to limit the amount of increase that can be obtained in cruise aerodynamic efficiency and the sensitivity of the grid size had a greater impact on the optimization of the airfoil section. The assumption that the airfoil section has little influence on the stability performance was confirmed. It was also found that rerunning the optimized designs with the highest resolution grids still maintained the improvements seen in the objective functions, further indicating the positive impact of the optimization process. The existence of non-linear characteristics in the yawing moment coefficient due to sideslip was found in all the winglet design cases. Detailed flow pattern investigations revealed the strong

destabilizing characteristics of the cockpit, centre fairing and the outer wing which was offset by the winglets' strong stabilizing behaviour. The inner wing displayed varying yaw characteristics going from the nominal to limiting sideslip conditions, due to large portions of separated regions found on the symmetric wing. The net effect of this is to reduce the yaw potential of the aircraft at high sideslip angles, causing the stall-like non-linear characteristics observed. The effect of the stability optimization was also correlated to flow characteristics on the winglet designs. Large separated regions of flow on the port side winglets' blend sections for all the designs were observed. Their magnitude was the primary contributing factor to the differences seen in the yaw stability derivatives. Additionally, a rudder control surface was parameterized for the Flying-V winglets for its potential use in RANS-based analysis and optimization taking into account realistic constraints such as hinge line definitions and lateral gaps. A preliminary analysis showed that the rudder was ineffective in stabilizing the aircraft at steady heading sideslip cases, but an uninvestigated, unexplained flow phenomenon causes the aircraft with rudders deflected to become extremely stable at limiting sideslip cases.

Chapter 7

Recommendations

The conclusions of this research indicated that the framework developed to perform the high-fidelity aerodynamic analysis and optimization of the winglets could be used to successfully gain improvements in the performance of the winglets. However, the potential exists to expand and improve upon some of the findings from the current study. A few recommendations are made for future researchers on the Flying-V. While the SU2 solver was validated using a representative geometry with similar flow conditions to the Flying-V, this operating condition was only representative of the cruise phase. It is still yet to be determined how the SU2 solver with similar settings performs when considering a representative case at the Flying-V's field conditions. The flow characteristics must include a high angle of attack scenario with largely separated regions of flows generating large amounts of lift. Additionally, the grid convergence of the stability coefficients must be verified using even higher cell mesh counts to provide more confidence to the solutions obtained for the stability performance of the Flying-V. The stability optimization included a fixed angle of attack scenario, rather than a fixed design lift coefficient scenario. This was because, one, the FV-1000 design could not reach the target lift coefficient at approach conditions at operationally practical angles of attack, and two, the version of SU2 that was used did not feature the fixed lift coefficient mode in sideslip conditions. Later versions of SU2 that include this feature and must be used in future studies for the approach condition performance analysis. It was also seen that the cruise angles of attack at which the design lift coefficient was generated were impractical for a realistic scenario. This could be reduced by using an optimized version of the FV-1000 for winglet optimization. The shock-induced separation at the wing tip could be mitigated by including the wing tip airfoil in the optimization process as it was seen that the planform shape could only solve this issue to an extent. The multi-objective optimization must also be conducted with airfoil parameters in the loop to check if the observation made that the stability parameters are not sensitive to airfoil optimization is true. This could be done with single steps and multi-steps and will also provide the influence of structural constraints on the airfoil shape on the stability performance. Ways to account for the non-linearities in the stability performance must be thought of if they are to be used in aerodynamic models or control models. Mesh issues causing non-zero side force and moments at zero sideslips must be investigated further. Just a preliminary elimination-based approach was taken to identify the source of the issue. Since the planform optimization step did not converge, likely due to the population size and the airfoil optimization having relatively low convergence criteria, both optimizations should be repeated by dedicating more run times. This should be done with higher-resolution grids. This should be done with a higher population and generation count (sample size) to allow the optimizer to converge and while also using a higher tolerance. A sensitivity analysis to find optimal sample space by varying the mutation, and recombination values along with different mutation strategies. The rudder design must be investigated further. Particularly, a grid convergence and sensitivity to solver settings for their RANS analysis. The geometry must be updated to span the full winglet, including the Kuchemann tip, as it now only

extends the winglet section. This can provide more area to the rudder section to maximize its effectiveness. Its performance at varying angles of attack, sideslip conditions and deflections must also be investigated as its potential to be used in a RANS analysis was shown. The effects of varying sizes of the gaps on the flow and effectiveness of the rudder must be investigated. The airfoil shape of the winglet also affects the rudder performance. This can be verified with a more detailed flow pattern investigation, and could then also be included in an optimization process to maximize directional control.

Bibliography

[1] Filburn, T. (2020). *Commercial Aviation in the Jet Era and the Systems that Make it Possible.* First edition, Springer, ISBN 978-3-030-20111-1.

[2] Lee, J. J., Lukachko, S. P., Waitz, I. A., and Schafer, A. (2001). *Historical and Future Trends in Aircraft Performance, Cost, and Emissions.* Annual Review of Energy and the Environment, 26(1), pp. 167-200. https://doi.org/10.1146/annurev.energy.26.1.167

[3] Liebeck, R. H. (2004). *Design of the blended wing body subsonic transport.* Journal of aircraft, 41(1), 10-25. https://arc.aiaa.org/doi/abs/10.2514/1.9084?casa_token=pYTuwbVWiEkAAAAA:VMfaIv5-0xXSam1RdrHKUsRXveY7ZXuf6BRivNVEoeUUnfsxX5SaAQAQ0SOiVQMFuPIboObOfuk

[4] Smith, H. (2000). *College of aeronautics blended wing body development programme.* In ICAS Congress (pp. 1-10). https://www.icas.org/ICAS_ARCHIVE/ICAS2000/PAPERS/ICA0114.PDF

[5] Bolsunovsky, A. L., Buzoverya, N. P., Gurevich, B. I., Denisov, V. E., Dunaevsky, A. I., Shkadov, L. M., and Zhurihin, J. P. (2001). *Flying wing—problems and decisions.* Aircraft design, 4(4), 193-219. https://www.sciencedirect.com/science/article/abs/pii/S1369886901000052?casa_token=NqKhlYCMtJMAAAAA:FYnttwXDCepGndfaHlTYcjmFovGh1uB_DlL6BT5pcwvJyYCC2Pt7MO8b5T2aQSZ3CclplDwRrw

[6] Benad, J. (2015). *The Flying V - A new Aircraft Configuration for Commercial Passenger Transport.* Deutsche Gesellschaft für Luft- und Raumfahrt - Lilienthal-Oberth e.V., urn:nbn:de:101:1-201511275089. https://doi.org/10.25967/370094

[7] Faggiano, F. (2016). *Aerodynamic Design Optimization of a Flying V Aircraft.* [Master's Thesis, TU Delft]. Education Repository. Retrieved from: http://resolver.tudelft.nl/uuid:0b1472a5-3aad-433c-9a64-242c84b114fd

[8] Hillen, M. (2020). *Parameterisation of the Flying-V Outer Mould Line.* [Master's Thesis, TU Delft]. Education Repository. Retrieved from: http://resolver.tudelft.nl/uuid:f4863ae4-2792-4335-b929-ff9dfdb6fed5

[9] Oosterom, W. (2021). *Flying-V Family Design.* [Master's Thesis, TU Delft]. Education Repository. Retrieved from: http://resolver.tudelft.nl/uuid:9e8f9a41-8830-405d-8676-c46bf6b07891

[10] van der Pluijm, R. (2021). *Cockpit Design and Integration into the Flying V.* [Master's Thesis, TU Delft]. Education Repository. Retrieved from: http://resolver.tudelft.nl/uuid:da4a8d74-32fa-45f1-9f92-d01d45fdea01

[11] Johnson, N. (2021). *Effect of Winglet Integration and Rudder Deflection on Flying-V Aerodynamic Characteristics.* [Master's Thesis, TU Delft]. Education Repository. Retrieved from: http://resolver.tudelft.nl/uuid:b664ae03-846f-4ad3-849a-c081a32260ad

[12] Cappuyns, T. (2019). *Handling Qualities of a Flying V Configuration.* [Master's Thesis, TU Delft]. Education Repository. Retrieved from [File Embargo - 17-12-2024]: http://resolver.tudelft.nl/uuid:69b56494-0731-487a-8e57-cec397452002

[13] European Aviation Safety Agency (EASA). (2019) *Certification Specifications and Acceptable Means of Compliance for Large Aeroplanes CS-25.* Amendment 23. https://www.easa.europa.eu/document-library/certification-specifications/cs-25-amendment-23

[14] Horwitz, J. M. T. (2021). *Parametric Design of the Flying-V Winglets for Improved Lateral-Directional Stability and Control.* [Master's Thesis, TU Delft]. Education Repository. Retrieved from: http://resolver.tudelft.nl/uuid:d7513b36-b9fd-4f8a-8726-f5c7ee7f3a6b

[15] Anderson Jr., J. D. (2010). *Fundamentals of Aerodynamics*. Fifth edition, McGraw Hill Incorporated. ISBN 0-07-0070012-5.

[16] Obert, E. (2009). *Aerodynamic Design of Transport Aircraft.* First edition, IOS Press BV. ISBN 978-1-58603-970-7.

[17] McLean, D. (2005). *Wingtip Devices: What They Do and How They Do It.* Boeing Performance and Flight Operations Engineering Conference, Article 4. https://www.smartcockpit.com/docs/Wingtip_Devices.pdf

[18] Whitcomb, R. (1976). *A Design Approach and Selected Wind Tunnel Results at High Subsonic Speeds for Wing-tip Mounted Winglets.* NASA Langley Research Center Hampton, Virginia, United States, NASA Technical Note D-8260. https://ntrs.nasa.gov/citations/19760019075

[19] Heyson, H. H., Riebe, G. D., and Fulton, C. L. (1977). *Theoretical parametric study of the relative advantages of winglets and wing-tip extensions.* NASA Langley Research Center Hampton, Virginia, United States, NASA Technical Memorandum X-74003. https://ntrs.nasa.gov/api/citations/19770010046/downloads/19770010046.pdf

[20] Engineering Sciences Data Unit (ESDU). (1998). *Aerodynamic principles of winglets.* Technical Report ESDU 98013. https://www.esdu.com/cgi-bin/ps.pl?sess=unlicensed_1210702114937zqs&t=doc&p=esdu_98013

[21] Derksen, R. W., and Rogalsky, T. (2010). *Bezier-PARSEC: An optimized aerofoil parameterization for design.* Advances in engineering software, 41(7-8), 923-930. https://www.sciencedirect.com/science/article/abs/pii/S0965997810000529?casa_token=XMYsJ8bRXIsAAAAA:WXNnUhe4LEjnzrJtBADa8QwvZpXWeL_6614BR8ILNTckUqssS5DBCdhcuI75X_FbfgU8ntG3hg

[22] Kroo, I. (2005). *Nonplanar wing concepts for increased aircraft efficiency.* VKI lecture series on Innovative Configurations and Advanced Concepts for Future Civil Aircraft. https://citeseerx.ist.psu.edu/viewdoc/download?doi=10.1.1.139.9694&rep=rep1&type=pdf

[23] Lanchester, F. W. (1907). *Aerodynamics.* Constable, London.

[24] Prandtl, L. (1918). *Tragflügeltheorie.* Königliche Gesellschaft der Wissenschaften zu Göttingen.

[25] Munk, M. M. (1923). *The minimum induced drag of aerofoils.*

[26] Nagel, F. (1924). *Wings With End Plates.* Engineering Division, McCook Field, Memorandum Report No. 130.

[27] Mangler, W. (1938). *The Lift Distribution of Wings With End Plates.* NACA Technical Memorandum No. 856. https://ntrs.nasa.gov/citations/19930094560

[28] Weber, J. (1954). *Theoretical Load Distribution on a Wing with Vertical Plates.* Aeronautical Research Council, Reports and Memoranda No. 2960. https://reports.aerade.cranfield.ac.uk/bitstream/handle/1826.2/3524/arc-rm-2960.pdf?sequence=1&isAllowed=y

[29] Chambers, J. R. (2003). *Concept to Reality: Contributions of the NASA Langley Research Center to U.S. Civil Aircraft of the 1990s.* NASA History Series, NASA Special Publication 2003-4529. https://ntrs.nasa.gov/api/citations/20030059513/downloads/20030059513.pdf

[30] Park, P., and Rokhsaz, K. (2003). *Effects of a winglet rudder on lift-to-drag ratio and wake vortex frequency.* In 21st AIAA Applied Aerodynamics Conference (p. 4069). https://arc.aiaa.org/doi/abs/10.2514/6.2003-4069

[31] Takenaka, K., Hatanaka, K., Yamazaki, W., and Nakahashi, K. (2008). *Multidisciplinary design exploration for a winglet.* Journal of aircraft, 45(5), 1601-1611. https://arc.aiaa.org/doi/pdf/10.2514/1.33031?casa_token=kKbbKZH7c5cAAAAA:Z7Rtd-lc8dgpfnCqPcJEyRvVIDGvqNIQdEm7zbYDdIsOP6Jn_Vh5zjsavNDrV7d4ixXHJ0Mj2us

[32] Veldhuis, L.L.M. (2018). *AE4130 - Aircraft Aerodynamics Assignment 5c.* Delft University of Technology.

[33] Jordan, D. L. and Gregory, J. M. (1993).*Winglets as a Directional Control Device* AIAA Journal, Vol. 31, No. 3, pp. 534-540.

[34] Sohovic, J. F. (1982). *The Effect of Winglets on Aircraft Handling Qualities* Proceedings of the 26th Annual Technical Meeting of the Society of Flight Test Engineers, pp. 357-370.

[35] Holmes, B. J., van Dam, C. P., Brown, P. W., and Deal, P. L. (1980). *Flight evaluation of the effect of winglets on performance and handling qualities of a single-engine general aviation airplane* (No. L-13960). https://ntrs.nasa.gov/api/citations/19810003504/downloads/19810003504.pdf

[36] Hageman, R. (2016). *Rudder Incorported Winglet Design for Blended Wing Body Aircraft* [Master's Thesis, TU Delft]. Education Repository. Retrieved from: http://resolver.tudelft.nl/uuid:404af9a0-17f2-45fc-bf41-9171e63b4e36

[37] Bourdin, P., Gatto, A., and Friswell, M. I. (2008). *Aircraft control via variable cant-angle winglets.* Journal of Aircraft, 45(2), 414-423. https://arc.aiaa.org/doi/pdf/10.2514/1.27720?casa_token=29wrdPMMY1AAAAAA:58uYAkpcQAYI_SGX7VwVTMovfFVQqjoyc-VJFYMVDLYR3AYYwBt02iNjqu70YREN8n_x_51xTMM

[38] Sobieszczanski-Sobieski, J., Morris, A., and Van Tooren, M. (2015). *Multidisciplinary Design Optimization Supported by Knowledge Based Engineering*. First edition, John Wiley & Sons. ISBN 978-1-118-49212-3.

[39] Brouwer, Y. (2022). *Constrained Aerodynamic Optimization of the Flying-V Nose Cone and Center-Body Fairing*. [Master's Thesis, TU Delft]. Education Repository. Retrieved from: http://resolver.tudelft.nl/uuid:4f9eea41-8dbc-4947-b599-46647b3e365b

[40] Luijk, N. V. (2023). *Constrained Aerodynamic Shape Optimisation of the Flying V Outer Wing.* [Master's Thesis, TU Delft]. Education Repository. Retrieved from: http://resolver.tudelft.nl/uuid:fc2bbe10-6796-4337-81cc-5971b324d50e

[41] Kulfan, B. M. (2008). *Universal parametric geometry representation method.* Journal of aircraft, 45(1), pp. 142-158. https://doi.org/10.2514/1.29958

[42] Natale, N., Salomone, T., De Stefano, G., and Piccolo, A. (2020). *Computational evaluation of control surfaces aerodynamics for a mid-range commercial aircraft.* Aerospace, 7(10), 139. https://doi.org/10.3390/aerospace7100139

[43] Streher, L. B., and Heinrich, R. (2021). *Meshing Strategy for Movable Control Surfaces: Towards High-Fidelity Flight Maneuver Simulations.* In New Results in Numerical and Experimental Fluid Mechanics XIII: Contributions to the 22nd STAB/DGLR Symposium (pp. 677-686). Springer International Publishing. https://doi.org/10.1007/978-3-030-79561-0_64

[44] Küchemann, D. (2012). *The aerodynamic design of aircraft.* American Institute of Aeronautics and Astronautics, Inc.. https://doi.org/10.2514/4.869228

[45] Galbraith, M. C., and Haimes, R. (2022). *A Parametric G1-continuous Rounded Wing Tip Treatment for Preliminary Aircraft Design.* In AIAA SCITECH 2022 Forum, pp. 1734. https://doi.org/10.2514/6.2022-1734

[46] Keller, D., and Rudnik, R. (2017). *Aerodynamic assessment of potential rudder force augmentation due to circulation control based on a VTP rudder design for a STOL aircraft*. (Doctoral dissertation, German Aerospace Center). https://elib.dlr.de/116058/1/C1_KellerRudnik.pdf

[47] Koeltzsch, K. (2000). *The height dependence of the turbulent Schmidt number within the boundary layer.* Atmospheric Environment, 34(7), pp. 1147-1151. https://doi.org/10.1016/S1352-2310(99)00369-6

[48] Palacios, F., Colonno, M. R., Aranake, A. C., Campos, A., Copeland, S. R., Economon, T. D., Lonkar, A. K, Lukaczyk, T. W., Taylor, T. W. R., and Alonso, J. J. (2013). *Stanford University Unstructured (SU2): An open-source integrated computational environment for multi-physics simulation and design.* 51st AIAA Aerospace Sciences Meeting including the New Horizons Forum and Aerospace Exposition, AIAA 2013-287. https://doi.org/10.2514/6.2013-287

[49] Spalart, P. R., and Allmaras, S. R. (1994). *A one-equation turbulence model for aerodynamic flows.* La Recherche Aérospatiale, 1-21. https://turbmodels.larc.nasa.gov/Papers/RechAerosp_1994_SpalartAllmaras.pdf

[50] Jameson, A. (2017). *Origins and further development of the Jameson–Schmidt–Turkel scheme.* AIAA Journal, 55(5), 1487-1510. http://aero-comlab.stanford.edu/Papers/jst_2015_updated_07_03_2015.pdf

[51] Saltelli, A., Ratto, M., Andres, T., Campolongo, F., Cariboni, J., Gatelli, D., and Tarantola, S. (2008). *Global sensitivity analysis: the primer.* John Wiley & Sons. https://web.archive.org/web/20180723161351id_/http://cds.cern.ch/record/1251806/files/9780470059975_TOC.pdf

[52] Greer, H. D. (1972). *Summary of directional divergence characteristics of several high performance aircraft configurations* No. NASA-TN-D-6993. https://ntrs.nasa.gov/citations/19730001306

[53] Smith, A. E., Coit, D. W., Baeck, T., Fogel, D., and Michalewicz, Z. (1997). *Penalty functions.* Handbook of evolutionary computation, 97(1), C5. https://citeseerx.ist.psu.edu/document?repid=rep1&type=pdf&doi=00376c2bd9d5045078135b7ea58380e46c7b0c12

[54] Storn, R., and Price, K. (1997). *Differential evolution-a simple and efficient heuristic for global optimization over continuous spaces.* Journal of global optimization, 11(4), 341.https://www.cp.eng.chula.ac.th/~prabhas//teaching/ec/ec2012/storn_price_de.pdf

[55] Schmitt, V. and Charpin., F. (1979). *Pressure Distributions on the ONERA-M6-Wing at Transonic Mach Numbers.* Experimental Data Base for Computer Program Assessment. Technical report, Fluid Dynamics Panel Working Group 04, AGARD AR-138. https://www.sto.nato.int/publications/AGARD/AGARD-AR-138/AGARD-AR-138.pdf

[56] Durrani, N., and Qin, N. (2011). *Comparison of RANS, DES and DDES results for ONERA M-6 Wing at transonic flow speed using an in-house parallel code.* 49th AIAA Aerospace Sciences Meeting including the New Horizons Forum and Aerospace Exposition, AIAA 2011-190. https://doi.org/10.2514/6.2011-190

Appendices

A Additional Data Used in Analysis and Optimization

Variable	Value
S_{ref} [m^2]	927.11
$\overline{c}_{ref}$ [m]	18.23
b_{ref} [m]	32.30
$I(x,z)$ $(\cdot e^7)$ [kg $\cdot$ m^2]	6.58, 3.96 [12]

Table 1: Reference Data for the FV-1000

Trajectory	r_b [m]	b [m]	λ [-]	Λ [°]	ϕ [°]	ϵ_r [°]	ϵ_t [°]
1	0.30	2.42	0.38	2.63	2.63	-2.57	13.42
2	1.24	10.00	0.76	50.00	18.84	8.68	15.00
3	2.50	6.21	1.00	44.74	50.00	-5.53	0.37
4	1.36	9.58	0.81	36.84	0.00	-15.00	-11.84
5	1.99	9.16	0.30	18.42	5.26	10.26	-15.00
6	0.61	5.37	0.43	0.00	26.32	0.79	10.26
7	1.74	2.00	0.95	23.68	21.05	15.00	3.95
8	0.85	4.25	0.85	7.64	42.98	-10.26	-5.98

Table 2: Design Trajectories - Winglet Design Variables Used in the Sensitivity Analysis

B Extensions to MMG Grid Generation Module

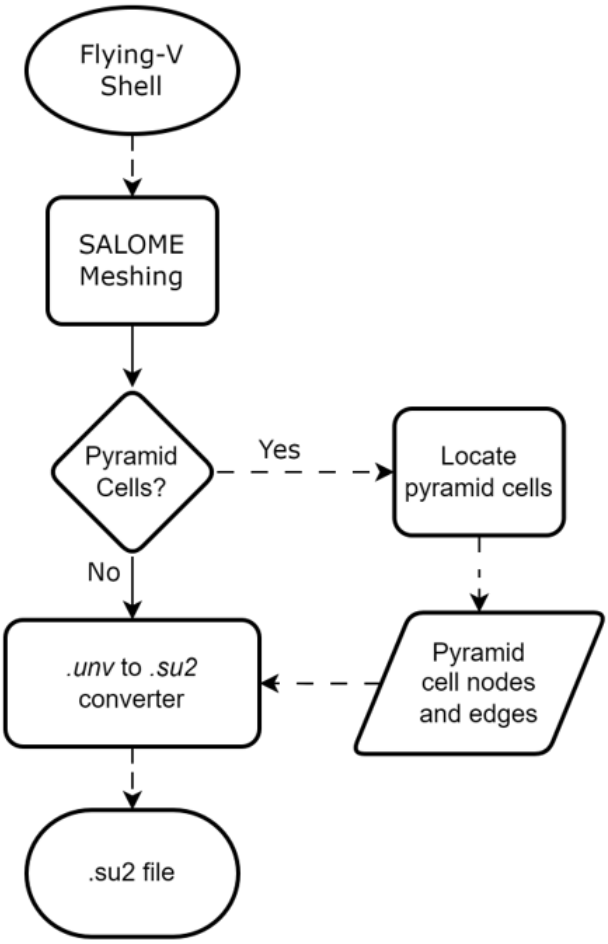

Figure 1: Process Flow to Identify Pyramid Cells in the SALOME Volume Mesh

C Supplemental Stability Polars

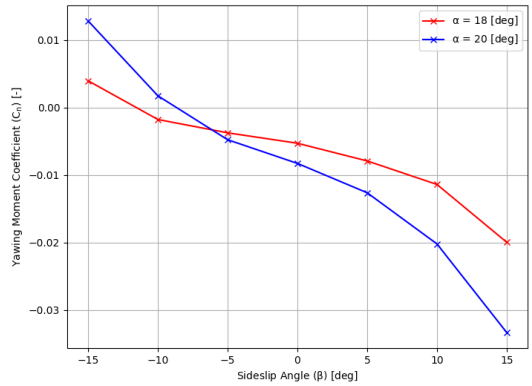

(a) Yawing Moment Coefficient

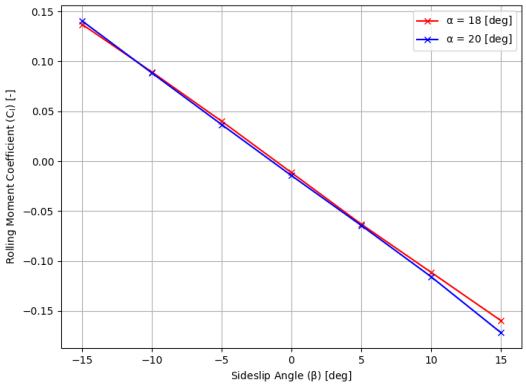

(b) Rolling Moment Coefficient

Figure 2: Comparison of Winglet-off Sideslip Polars of Stability Coefficients for Varying Angles of Attack (M = 0.22 [-])

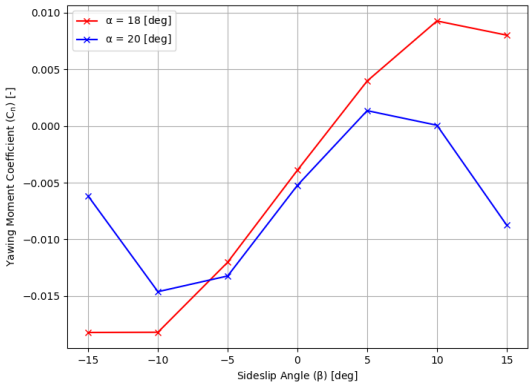

(a) Yawing Moment Coefficient

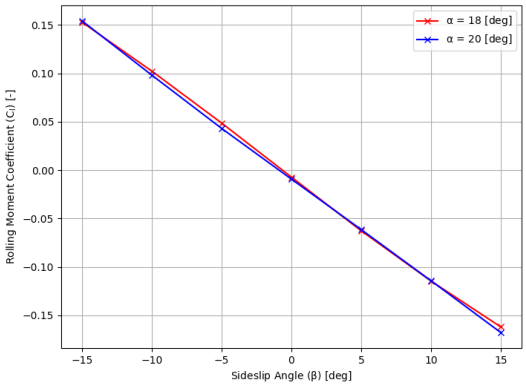

(b) Rolling Moment Coefficient

Figure 3: Comparison of Legacy Winglet Sideslip Polars of Stability Coefficients for Varying Angles of Attack (M = 0.22 [-])